IEEE Access
Multidisciplinary ⋮ Rapid Review ⋮ Open Access Journal

Received 20 September 2023, accepted 17 October 2023, date of publication 20 November 2023,
date of current version 27 November 2023.

Digital Object Identifier 10.1109/ACCESS.2023.3334606

RESEARCH ARTICLE

Doppler Shift and SFO Robust Synchronization for LoRa-Like Acoustic Underwater Communication

FABIAN STEINMETZ, (Graduate Student Member, IEEE), AND BERND-CHRISTIAN RENNER
Institute for Autonomous Cyber-Physical Systems, Hamburg University of Technology (TUHH), 21079 Hamburg, Germany

Corresponding author: Fabian Steinmetz (fabian.steinmetz@tuhh.de)

This work was supported by the Funding Programme Open Access Publishing of the Hamburg University of Technology (TUHH).

ABSTRACT Frequency shift chirp modulation (FSCM) is the modulation technique utilized by the LoRa physical layer, a widely used and relatively new communication technique for radio low-power wide area networks (LPWANs). In this paper, we adapt and implement FSCM for low-power acoustic underwater communication. Opposed to over-water communication based on the electromagnetic wave, the acoustic wave in water travels much slower. Consequently, acoustic underwater communication is more sensitive to motion-based Doppler shifts. For resilient acoustic underwater communication, Doppler tracking and removal is mandatory. In this paper, we mathematically derive the effect of Doppler shifts to FSCM symbols. Afterwards, we describe a novel algorithm for a low-power receiver to track Doppler shifts without modification of the transmitted packet. Finally, we evaluate and compare our algorithm to another Doppler estimation algorithm from literature and study the effect on the bit error rate (BER). We show, that our algorithm can improve with little additional computational overhead the BER by a factor of more than 10^4 in some cases.

INDEX TERMS LoRa, FSCM, Doppler, underwater communication, underwater wireless sensor network, ahoi modem.

I. INTRODUCTION

In the last years, many research groups investigated new LPWANs for the over-water Internet of Things (IoT), especially LoRaWAN. LoRaWAN is composed of a physical (PHY) layer, the LoRa-PHY (frequently called LoRa) and a medium access control (MAC) layer. However, the LoRa-PHY is a proprietary standard and details of the implementation are unspecified. Therefore, numerous papers have been published on demodulating LoRa packets, e. g., [1], [2], and [3]. Based on these publications, the principles of the modulation and demodulation are known and the modulation is named FSCM in many papers [4]. A FSCM receiver requires a precise synchronization, which is covered by several studies, e. g., [5], [6], and [7]. During the synchronization, the receiver has to estimate and compensate different offsets: symbol timing offset (STO), carrier frequency offset (CFO), and sampling frequency offset (SFO) [5], [8]. STO describes the time difference between the assumed and real symbol boundaries, CFO the frequency difference between the carrier frequency oscillators of the transmitter and receiver, and SFO the sampling frequency difference between transmitter and receiver.

In our research, we adapt and implement FSCM for low-power acoustic underwater communication. Similar to the over-water IoT, the Internet of Underwater Things (IoUT) is a rising research topic [9], [10]. Figure 1 illustrates typical applications, for example swarm communication for micro autonomous underwater vehicles (μAUVs), e. g., [11], [12], and [13] or underwater wireless sensor networks (UWSNs), e. g., [14], [15], [16], and [17]. Furthermore, acoustic underwater communication is part of the vision for 6G wireless networks [18], [19], the next-generation of wireless networks. Therefore, proper modulation schemes for underwater communication are required.

In [20], we presented a FSCM scheme for acoustic underwater communication with low-power acoustic modems, e. g., the *ahoi* modem [21] or the FAU modem [22].

The associate editor coordinating the review of this manuscript and approving it for publication was Mohamed M. A. Moustafa.

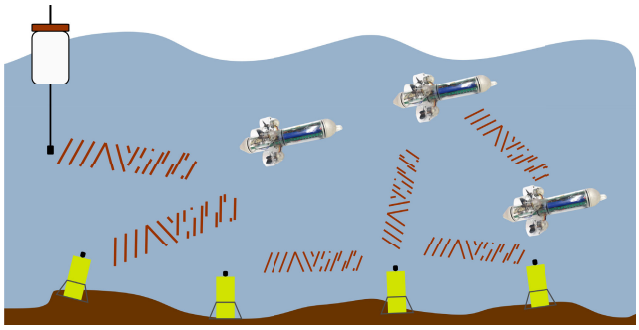

FIGURE 1. Acoustic FSCM for the IoUT. For example for swarm communication or underwater sensor nodes.

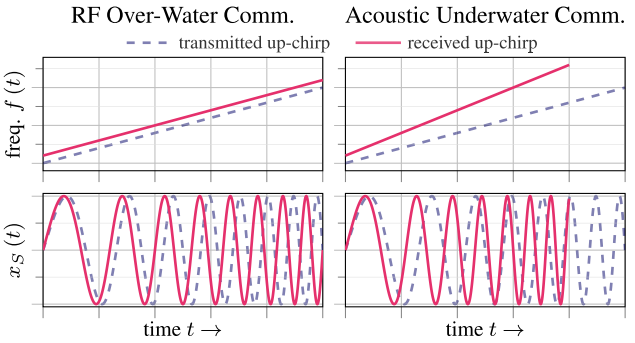

FIGURE 2. Effect of Doppler Shifts on linear modulated frequency shift (up-chirp) in RF over-water communication and acoustic underwater communication.

Acoustic communication is preferably used underwater due to the strong attenuation of the electromagnetic wave in the water. Opposed to the electromagnetic wave in radio frequency (RF) systems, which travels with the speed of light $c_{\text{light}} \approx 3 \times 10^8$ m/s, the acoustic wave in water is much slower with a speed of sound $c_{\text{sound}} \approx 1500$ m/s.

Another aspect of acoustic underwater communication is that the carrier frequency f_c is in the same order of magnitude as the bandwidth BW due to the properties of the acoustic channel. For example, the first underwater communication standard JANUS [23] uses BW $\approx f_c/3$. Default JANUS values are $f_c = 11.52$ kHz, BW $= 4.16$ kHz. In [20], our FSCM scheme has $f_c = 62.5$ kHz, BW $= 20$ kHz. Typically, over-water LoRa has $f_c \in \{433\,\text{MHz}, 868\,\text{MHz}, 915\,\text{MHz}, 2.4\,\text{GHz}\}$ and BW $\in \{125\,\text{kHz}, 250\,\text{kHz}, 500\,\text{kHz}\}$ [24].

As a consequence, the main difference between FSCM-based over and underwater communication w. r. t. Doppler Shifts, CFO and SFO are[1]:

- In **over-water communication** systems $fc \gg$ BW and the received signal is sampled in the base band (BB). Therefore, SFO affects the BB signal. CFO occurs due to carrier clock frequency differences between transmitter and receiver. For small velocities Doppler shifts can be assumed as constant over the bandwidth and considered as CFO, because the carrier frequency is much higher than the bandwidth.
- In **underwater communication** systems $fc \approx$ BW and many modems sample the signal in the pass band (PB). Afterwards, the signal is shifted to the BB in software. SFO occurs in the PB signal and CFO does not affect the signal. Doppler shifts are frequency-dependent over the transmission bandwidth and more dominant compared to over-water communication.

Figure 2 illustrates the different effect of Doppler shifts for a linear modulated frequency shift (up-chirp). In the case of RF-based over-water communication the carrier frequency is circa 10^4 higher and the propagation speed circa 10^5 faster compared to acoustic underwater communication. On the other hand, the bandwidth is circa 10^3 smaller compared to the carrier frequency in over-water communication. In underwater communication bandwidth and carrier frequency are in the same order. For over-water communication the chirp has approximately a constant frequency shift in Fig. 2. Opposed to that, the frequency varies over the time in acoustic underwater communication and the signal is compressed in the time domain.

[1] in Section II and Section III we discuss the assumptions in more detail.

CONTRIBUTIONS AND ORGANIZATION

In this paper, we discuss and counter Doppler shifts and SFO for acoustic underwater communication. First, we review other synchronization algorithms in Section II. Afterwards, we describe acoustic underwater channels and derive the effect of STO, SFO, and Doppler shifts to a FSCM signal in Section III. Furthermore, we present an efficient synchronization in Section IV to estimate Doppler shifts and describe a Doppler shift resilient receiver. At last, we evaluate our findings in Section V. We show that our new implementation can improve the BER from circa 10^{-1} (without Doppler removal) to less than 10^{-5} (with Doppler removal and additional modifications) at a relative velocity of 0.75 m/s respectively from circa 10^{-1} to 10^{-4} at 1.5 m/s. These velocities are common for low-cost underwater vehicles, e. g., the widely used BlueROV2 has a maximum velocity of 1.5 m/s [25].

It is important to note, that our findings are also relevant for RF systems. Many papers tried to study Doppler effects based on field trials with different results, e. g., [26], [27], and [28]. Our paper provides a mathematical foundation to increase the understanding. Moreover, Doroshkin et al. [26] studied FSCM for satellite to earth communication. In this case, Doroshkin et al. simulated relative velocities up to 3×10^4 m/s, where the Doppler shift is comparable to 0.15 m/s in the case of acoustic underwater communication. The following methods can be easily adapted to satellite to earth communication.

II. RELATED WORK

This section reviews existing publications and is divided into three parts. First, experimental RF studies are covered in

TABLE 1. Summary of the related work section. Related work starts with experimental studies, then covers SDR implementation for RF and finally lists all existing frequency shift chirp modulation (FSCM) for acoustic underwater communication. abbreviations: software defined radio (SDR), symbol timing offset (STO), carrier frequency offset (CFO), sampling frequency offset (SFO), radio frequency (RF), underwater communication (UWC), matched filter (MF).

Authors	Year	Medium	Pract. Velo.	SDR	Int. STO	Frac. STO	Int. CFO	Frac. CFO	SFO / Doppler	Remarks
Petäjäjärvi *et al.* [27]	2017	RF	✓	-	-	-	-	-	-	
Patel and Won [28]	2017	RF	✓	-	-	-	-	-	-	
Liando *et al.* [3]	2019	RF	✓	-	-	-	-	-	-	
Doroshkin *et al.* [26]	2019	RF	✓	-	-	-	-	-	-	
Ameloot *et al.* [29]	2021	RF	-	(✓)	-	-	-	-	-	
Knight and Seeber [1]	2016	RF	-	✓	✓	-	-	-	-	
Robyns *et al.* [30]	2018	RF	-	✓	✓	-	✓	-	✓	Blind estimation of SFO and re-alignment during demodulation
Ghanaatian *et al.* [2]	2019	RF	-	✓	✓	-	-	✓	✓	Monte-Carlo simulation to study the effect of SFO
Bernier *et al.* [5]	2020	RF	-	✓	✓	-	✓	✓	-	
Ben Temim *et al.* [31]	2020	RF	-	✓	✓	✓	(✓)	(✓)	-	
Tapparel *et al.* [32]	2020	RF	-	✓	✓	✓	✓	✓	-	
Chen *et al.* [8]	2021	RF	-	(✓)	-	-	-	-	-	
Xhonneux *et al.* [7]	2022	RF	-	✓	✓	✓	✓	✓	-	
Rezzouki *et al.* [33]	2021	UWC	-	✓	✓	✓	(-)	(-)	✓	Doppler detection with 1 s long chirp
Steinmetz and Renner [20]	2022	UWC	-	✓	✓	-	(-)	(-)	-	
Rezzouki and Ferré [34]	2022	UWC	-	✓	✓	✓	✓	✓	✓	Doppler detection with 1 s long chirp
Jia *et al.* [35]	2022	UWC	-	✓	✓	-	(-)	(-)	-	MF for demodulation instead of dechirping
This paper	2023	UWC	-	✓	✓	✓	(-)	(-)	✓	

Section II-A. Afterwards, in Section II-B different software defined radio (SDR) for RF are discussed w. r. t. the synchronization process. Furthermore, Doppler shift estimation and compensation and FSCM for acoustic underwater communication are reviewed in Section II-C. The order traces the research progress, first existing receivers were explored with experimental studies followed by SDR implementations for RF applications. During the last two years, first research on acoustic FSCM was published.

A. ANALYSIS AND EXPERIMENTAL STUDIES

Since Semtech had launched the first commercially available RF LoRa transceiver in the year 2013 [36] and the LoRa Alliance was founded in 2015 [37], researchers started to explore the properties of LoRa and LoRaWAN with experimental studies. Petäjäjärvi et al. [27] compared the channel coherence time to the symbol duration. The coherence time describes the channel variation of the transmission channel and is typically defined by the inverse of Doppler shift. If the coherence time is longer than the symbol duration, the channel is classified as a fast fading channel. The spreading factor SF defines the number of bits modulated to a symbol in FSCM. They pointed out, that a lower SF results in a shorter symbol duration and tolerates therefore higher Doppler shifts. In their experiments, Petäjäjärvi et al. installed a transmitter on a car and measured the packet reception rate (PRR) for different distances up to 2400 m and different relative speeds between transmitter and receiver from up to 23.0 m/s. The setup was SF = 12, BW = 125 kHz, and f_c = 868 MHz. In static scenarios, they measured PRRs up to 98.9 %. Opposed to that, during the mobile measurement the PRR went down to 28.0 % on average. Patel and Won [28] conducted similar experiments with comparable results. However, they used the adaptive data rate (ADR) option of LoRaWAN, which controls bandwidth and spreading for an optimal throughput and energy consumption. At a distance of 805 m, they measured circa 99 % PRR in static scenarios and 61 % respectively 55 % at 2.2 m/s and 6.7 m/s vehicle speed. The vehicle traveled on a circular test track and the distance was measured to the center of the test track. Liando et al. [3] presented a short study with SF = 12. The transmitter was mounted on a car, which had a speed between 13.9 m/s to 22.2 m/s. They measured a PRR above 85 % for all speeds. Doroshkin et al. [26] described LoRa for satellite to earth communication for nanosatellites in low Earth orbit. It is a challenging transmission channel with relative velocities up to 8×10^3 m/s. At first, Doroshkin et al. used an SDR to generate packets with Doppler shifts and a commercial receiver. In all cases, they used f_c = 434 MHz. For example PRR above 70 % was measured for SF = 7, BW = 125 kHz and 255 B payload (0.55 s packet duration) at less than 21.3×10^3 m/s, or for SF = 12, BW = 125 kHz and 59 B payload (2.7 s packet duration) at less than 16.5×10^3 m/s. Furthermore, Doroshkin et al. performed real-world evaluations. The transmitter was mounted on a car. In all cases, the relative speed was between −33.3 m/s to 33.3 m/s and they measured PRRs above 97.2 % and packet loss only occurs in non-line-of-sight (NLOS) constellations. Ameloot et al. [29] characterized the Doppler effect on body-centric links with relative acceleration between transmitter and receiver. The

relative acceleration results in variable Doppler shifts during the packet reception. At first, they discussed a constant Doppler shift and used their own SDR [6] implementation for the evaluation. They showed, that a CFO synchronization and compensation improves the resilience against Doppler shifts.

In a nutshell, [27], [28] measured a strong impact of relative velocities between transmitter and receiver. Opposed to that, [3], [26], [29] showed a strong resilience against Doppler shifts. It is important to note, that [28] used the ADR option. Based on the LoRaWAN documentation, the ADR option should be used in static scenarios [38]. Presumably, the strong impact of velocity in [28] is the effect of an incorrect configuration. In summary, the discussed research papers support the conclusion that LoRa with CFO synchronization is resilient against Doppler shifts in RF-based over-water communication. However, a mathematical description of the effect of Doppler shifts w. r. t. the dechirping process is not provided in any of these papers.

TABLE 2. Methods for estimating the Doppler shift in acoustic underwater communication. abbreviations: binary phase shift keying (BPSK), quadrature phase shift keying (QPSK), binary frequency shift keying (BFSK), frequency shift chirp modulation (FSCM), matched filter (MF), phase-locked loop (PLL), linear frequency modulation (LFM).

Authors	Year	Data Mod.	Doppler Estimation
Johnson *et al.* [41]	1997	QPSK	Bank of MFs with shifted versions of a training signal and PLL
Sharif *et al.* [42]	2000	BPSK or QPSK	LFM chirp at begin and end of a packet
Zappa *et al.* [43]	2011	BFSK (JANUS)	Frequency shift of three wake-up tones
Diamant *et al.* [44]	2012	—	Up-chirp and down-chirp method with MFs
Baldone *et al.* [45]	2020	BFSK (JANUS)	Bank of MFs with shifted versions of a m-sequence
Rezzouki *et al.* [33], [34]	2021, 2022	FSCM	Fractional Fourier transform of a 1 s long LFM chirp
This Paper	2023	FSCM	Nyquist-rate receiver with dechirping of up- and down-chirps

B. SOFTWARE DEFINED RADIO (SDR) IMPLEMENTATIONS

In 2016, Knight and Seeber [1] presented one of the first open SDR implementations to receive LoRa packets focusing on STO only. Robyns et al. [30] estimated STO and CFO during the synchronization, however, SFO was not taken into account. Robyns et al. implemented a technique involving oversampling and a blind estimation of the SFO at the beginning of the data demodulation. During the demodulation SFO can be detected and corrected. In addition, the resolution of the SFO corrections is increased by oversampling. However, the method proposed by Robyns et al. only works for small SFO values. Opposed to that, Ghanaatian et al. [2] presented a non-coherent Nyquist-rate receiver with dechirping and analyzed the effect of CFO and SFO. Ghanaatian et al. showed that CFO has a strong impact on the BER. During the synchronization, only the fractional (residual) CFO was compensated. In general CFO leads to a time offset in synchronization when using only up-chirps, but the same offset affects the symbol detection. This method results in inter-symbol interference (ISI). In the case of a fractional CFO compensation, the BER decreased. In addition, a SFO also increased the BER. To avoid a complex re-sampling, Ghanaatian et al. changed the reference chirp w. r. t. the SFO. In addition, they countered the drift with discarding samples in combination with oversampling. Their receiver had an a-priory knowledge of the SFO and no SFO estimation was used. A comprehensive discussion of STO, CFO, and SFO can be found in Bernier et al. [5]. They described the effects of both the integer and fractional parts of these offsets.

Indeed, in the implementation and evaluation of non-coherent Nyquist-rate receiver with dechirping Bernier et al. compensate integer STO and the integer and fractional part of the CFO. Ben Temim et al. [31] presented a differential symbol coding based on FSCM. In this case, the information is transmitted in the difference between two symbols and not in a single symbol. They proposed a non-coherent Nyquist rate receiver with dechirping, which estimates fractional CFO and STO (integer and fractional parts). The integer CFO was omitted, because it effects all symbols in the same manner and is canceled out by differential coding. The signal was oversampled by factor of ten to remove fractional parts after the synchronization. Furthermore, Ben Temim et al. used a packet format without down-chirps. It is important to note, that this method is not compatible to the common LoRa modulation. Tapparel et al. [32] implemented an open source SDR based on GNU radio. During synchronization, they compensated integer and fractional STO and CFO. At first, integer STO was removed by a time shift and integer CFO with a frequency shift. Afterwards, fractional parts were estimated with the method from Yang et al. [39]. In this case, an upsampling of two was required. The fractional CFO was removed with an additional frequency shift and fractional STO with interpolation in the time domain. In Chen et al. [8], the authors described the effect of STO, CFO, and SFO including a synchronization algorithm. To estimate the SFO, Chen et al. examined the difference between left and right bin around the maximum of the fast Fourier transform (FFT) and tuned the local dechirp signal generator for compensation. However, an evaluation of the synchronization and demodulation was not presented. Xhonneux et al. [7] presented a non-coherent Nyquist-rate receiver with dechirping. During the synchronization, integer and fractional STO and CFO were removed. At first, fractional CFO is removed by tuning the local dechirp signal generator. Then the fractional STO was estimated based on a modified version of the algorithm from Jacobsen and Kootsookos [40] and removed. The signal was oversampled by a factor of ten, which allowed a simple realignment of baseband signal to remove fractional STO. At last, the integer STO and CFO were removed and the fractional STO

estimate were fine-tuned. In Xhonneux et al., the authors compared their results with those of Bernier et al. and showed that omitting the fractional STO led to improved receiver performance and lower BER.

In sum, many research groups presented SDR implementations. Most of them focused fractional and integer STO and CFO estimation and removal, whereas glssfo has been rarely discussed. To date, no algorithm has been presented that can estimate and compensate SFO and Doppler shifts.

C. ACOUSTIC UNDERWATER COMMUNICATION

In acoustic underwater communication systems, the wave travels with the speed of sound $c_{\text{sound}} \approx 1500\,\text{m/s}$, which is much slower than electromagnetic waves in RF systems. Based on that, Doppler shifts have a strong impact on acoustic underwater communication due to their relation w. r. t. the wave propagation speed. They were frequently discussed in literature, e. g., [46] and [47]. For example, a relative speed between receiver and transceiver of 0.5 m/s in acoustic underwater communication produces similar Doppler scaling compared to a relative speed of 10^5 m/s in RF communication.

Johnson et al. [41] used a bank of matched filters (MFs) with Doppler shifted versions of a training signal. The highest result of the MFs were used as a coarse Doppler shift estimation. Afterwards, a phase-locked loop (PLL) and an equalizer was used for fine adjustments. To estimate and compensate Doppler shifts, Sharif et al. [42] added a linear frequency modulation (LFM) chirp at the beginning and end of a packet. With a MF both chirps were detected and Doppler shifts were estimated due to the fact, that the Doppler effect decreased or increased the packet length. Afterwards, Sharif et al. resampled the packet with interpolation. Zappa et al. [43] used the three optional wake-up tones at the begin of a JANUS packet to estimate the Doppler shift. Zappa et al. used JANUS version 1 where a JANUS packet contains of three wake-up tones, a hyperbolic frequency modulation (HFM) chirp for time synchronization, and binary frequency shift keying (BFSK) modulated data. After the reception of the HFM sweep, the Doppler shifts of the wake-up tones were calculated. Finally, the Doppler shift was removed with re-sampling. Diamant et al. [44] introduced the up-down method, where an up-chirp is followed by a down-chirp. The Doppler shift was calculated based on the peak difference of the MFs. They tested their method with LFM and HFM chirps. Baldone et al. [45] implemented a Doppler shift tracking for JANUS version 2, in which the HFM chirp was replaced by a m-sequence of 32 pseudo-random symbols as a preamble. Comparable to Johnson et al., Baldone et al. used a bank of MFs with Doppler shifted versions of the preamble for joint estimation of the Doppler shift and time synchronization. The implementation was stable for relative speeds of up to 5 m/s.

An overview of the discussed methods is provided in Table 2. The methods presented in [41], [42], and [45] are challenging for low-power devices with limited computational resources and limited memory. In the case of [41] and [45], a bank of MFs come with high computational costs. For the method in [42], the receiver has to store the samples of the entire packet, because the Doppler shift is estimated after the reception of the chirp at the end of the packet. In addition, a real-time implementation is impossible, because the signal processing starts after the end of the packet. The algorithm presented in [43] requires additional constant frequency tones. Opposed to that, the algorithm in [44] is less complex and a promising solution for low-power implementations.

During the last years, chirp spread spectrum (CSS) was already used in acoustic underwater communication, e. g., for synchronization [42], [43], [48], [49], [50], data modulation [14], [51], [52] or sweeped carrier frequency [53], [54]. However, FSCM was actually rarely used for acoustic underwater communication. To the authors' best knowledge, four publications cover acoustic underwater FSCM.

Rezzouki et al. [33] used FSCM for an underwater communication and localization system. They introduced many concepts without going into the details and without evaluating the benefits of the signal processing steps. In all cases, an acoustic packet started with an 1 s long up-chirp, followed by a preamble of 20 shorter up-chirps and 20 down-chirps. Afterwards the data was transmitted. Rezzouki et al. used a differential data coding comparable to Ben Temim et al. (c. f. Section II-B). All chirps had a bandwidth of 5 kHz. At first, Rezzouki et al. used fractional Fourier transform of the 1 s long chirp for the estimation of the Doppler shift. Afterwards, the packet was resampled to remove the Doppler shift. The integer STO was removed by averaging over the dechirping peaks of all preamble symbols (20 up-chirps and 20 down-chirps). Finally, the 20 up-chirps were used to estimate the fractional STO. To counter multipath, Rezzouki et al. used an equalizer and toggle the spreading factor inside the payload. The evaluation took place in a simulator, which simulated a Doppler Shift, multipath propagation and additive white Gaussian noise (AWGN). In their subsequent publication, Rezzouki and Ferré [34] revealed further details and insights. Compared to [33], they used less preamble chirps (8 up-chirps and 2 down-chirps) and included a CFO estimation.

We (Steinmetz and Renner [20]) presented the first version of our FSCM system using a MF for synchronization and non-coherent Nyquist-rate receiver with dechirping for data demodulation. In [20], we considered integer STO only. For evaluation, we replayed acoustic underwater channel impulse responses using Watermark [55] and compared the BERs to JANUS. The channel impulse responses were measured in challenging conditions with strong multipath propagation [56]. In addition, we included a short real-world trial. Doppler shifts were not considered. Jia et al. [35] compared different CSS including FSCM. They implemented a MF for data demodulation and evaluated the BER w. r. t. noise resilience and multipath stability. However, similar to

our work, Jia et al. also neglected the impact of Doppler shifts.

In this paper, we extend our receiver from [20] and present a novel method for a joint estimation of Doppler shifts (respectively SFO) and STO based on Nyquist-rate receiver with dechirping. Integer and fractional STO are calculated. For compensating Doppler shifts and STO, we compare interpolation to a cost-efficient alignment in the transmission band (inspired by Ghanaatian et al.). Furthermore, we show that differential coding (inspired by Ben Temim et al.) can improve the resilience against Doppler shifts. Finally, we present a Doppler shift resilient packet scheme with different spreading factors for synchronization and data transmission.

III. ANALYTICAL DESCRIPTION OF THE EFFECT OF STO, CFO, SFO AND DOPPLER SHIFTS TO THE FSCM

The following section derives the effect of STO, SFO and Doppler shifts to the FSCM. It starts with an introduction into FSCM, the definition of offsets and receiver structures. Finally it characterizes STO, SFO and Doppler shifts.

A. OVER-WATER VS. UNDERWATER COMMUNICATION

The electromagnetic wave, typically used in over-water RF communication, is not suitable in most of applications of underwater communication due to the strong attenuation inside water. Commercial available RF transceivers can be used for transmission ranges over a few meters in the water. The authors in [57] used LoRaWAN with a slightly submerged sensor node and a gateway outside of the water. The communication link was stable, when the node was a few centimeter below the water surface. Other techniques are magneto inductive, optical and acoustic underwater communication [9]. Magneto inductive communication has a high power consumption and optical communication requires good visibility and low ambient light. Therefore, acoustic underwater communication is the most used communication technique.

The acoustic wave travels with a speed of sound of circa $c_{\text{sound}} = 1500\,\text{m/s}$, it depends on temperature, pressure (depth) and salinity [58]. The low propagation speed results in large transmission latencies, which are challenging for network protocols [59], [60]. A transmitted acoustic signal is affected by attenuation, noise, multipath propagation, and Doppler shifts before the reception at the receiver [46].

1) ACOUSTIC UNDERWATER COMMUNICATION: PATH LOSS

The overall path loss $L(d,f)$ depends on frequency f and distance d w. r. t. a reference distance d_0 (typical 1 m):

$$L(d,f) = \underbrace{20 \cdot n \cdot \log_{10}(d/d_0)}_{\text{spread loss } L_{\text{spr}}(d) \text{ in dB}} + \underbrace{(d-d_0) \cdot \alpha(f)}_{\text{absorption loss } L_{\text{abs}}(d,f) \text{ in dB}} \tag{1}$$

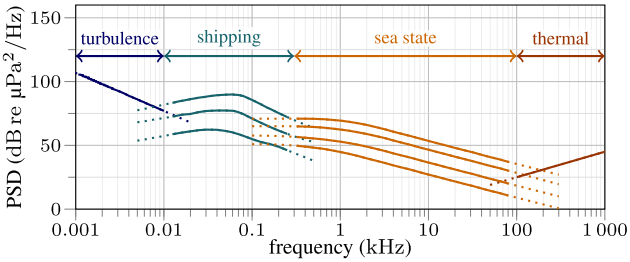

FIGURE 3. Acoustic background ambient noise. The noise is calculated with the equations and tables from [62] and [63] and is based on the diagram in [64]. Far shipping noise is shown with different shipping activity levels (heavy, moderate and light far shipping activity) and sea state noise for wind speeds of 0-1 knot, 4-6 knots, 11-16 knots, and 28-40 knots.

The spread loss $L_{\text{spr}}(d)$ depends on distance and spreading factor n, which describes the environment. For a spherical spreading and a free-field assumption $n = 1$ and $n = 0.5$ for a cylindrical wave. The frequency-dependent absorption loss coefficients $\alpha(f)$, calculated with Thorp's formula [61], are for example 6.1 dB/km (25 kHz), 17.5 dB/km (50 kHz), 27.1 dB/km (75 kHz), and 34.1 dB/km (100 kHz). The absorption loss is a result of the transfer of acoustic energy into heat.

2) ACOUSTIC UNDERWATER COMMUNICATION: ADDITIONAL NOISE

The acoustic background noise varies over the frequency range and is discussed in [46], [64], and [61]. In the frequency range between 1 Hz and 10 Hz ocean turbulence is the dominant noise source. Far shipping noise dominates at frequencies 10 Hz to 300 Hz. At higher frequencies, the sea state, caused by wind and waves, produces acoustic noise in the region between 300 Hz and 100 kHz. Thermal noise affects the region between 100 kHz and 1 MHz. The power spectral densities (PSDs) of different background noise sources and levels are depicted in Fig. 3. In addition to that, local noise sources, e. g., echosounders, near vessels or underwater robots, disturbs the received signal. The simulation of noise from vessels and autonomous underwater vehicles (AUVs) is described in [65]. In [17], an additional acoustic noise from the thrusters of the unmanned surface vehicle (USV) was observed during the real-world trials.

3) ACOUSTIC UNDERWATER COMMUNICATION: MULTIPATH PROPAGATION

Reflections at surface, sea bottom and other objects in the water result in a multipath propagation channel. The received signal $y(t)$ is [66]

$$y(t) = \int_{-\infty}^{\infty} h(t,\tau)\, x(t-\tau)\, \mathrm{d}\tau + n(t) \tag{2}$$

with the transmitted signal $x(t)$, additional noise $n(t)$, and

$$h(t,\tau) = \sum_{n=1}^{N} a_n(t)\, \delta(\tau - \tau_n)\,. \tag{3}$$

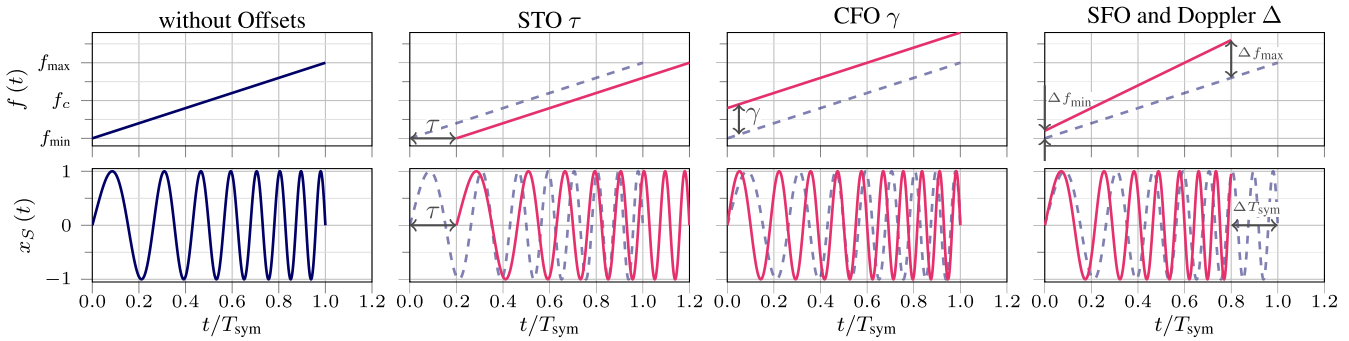

FIGURE 4. Effect of symbol timing offset (STO), carrier frequency offset (CFO), sampling frequency offset (SFO), and Doppler shift on an up-chirp $x_S(t)$ with symbol length T_{sym}, bandwidth BW, carrier frequency f_c and therefore an instantaneous frequency $f(t)$ (c. f. Eq. (7)) from $f_{min} = f_c - BW/2$ to $f_{max} = f_c + BW/2$.

$h(t, \tau)$ is the time-dependent transfer function of the acoustic channel, N the number of propagation paths, $a_n(t)$ the path gains, τ_n the path delays. Different measured acoustic underwater channels are shown in [47]. Especially in shallow water scenarios, e. g., ports or lakes, massive multipath propagation can be observed [56], [67].

4) ACOUSTIC UNDERWATER COMMUNICATION: DOPPLER SHIFTS

In the case of a relative speed v_0 between transmitter and receiver, the observed frequency f_y is different to the transmitted frequency f_x (Doppler shift) and is given by

$$f_y = \left(1 + \frac{v_0}{c_{\text{sound}}}\right) f_x \,. \tag{4}$$

In the time domain, the received signal is compressed or stretched

$$y(t) = x\left(\left(1 + \frac{v_0}{c_{\text{sound}}}\right) t\right) \,. \tag{5}$$

It is important to note, that Eq. (5) is valid without multipath propagation only. In the case of multipath propagation, each path has a different Doppler shift. The Doppler shift per path depends on the variation of the path length. Movements of reflectors, e. g., waves, generate additional shifts on single propagation paths.

5) COMPARISON TO THE OVER-WATER RF CHANNEL

Spreading loss, multipath propagation and Doppler shifts are also part of the over-water RF transmission channel. Similar to underwater transmission, the RF channels show a wide variation based on the application, environment and frequency bandwidth [19]. On the other hand, the frequency-dependent absorption loss of the acoustic underwater channel limits the usable frequency range. The absorption loss increases with frequency, which requires higher transmission gains at higher frequencies to achieve comparable receive signal strengths to those at lower frequencies. Furthermore, the propagation speed of the acoustic underwater channel (1500 m/s) is five orders of magnitude smaller than the speed of light (3×10^8 m/s), the propagation speed of the electromagnetic wave. Due to the frequency-dependent absorption loss, typical acoustic underwater transmission systems use carrier frequencies below 100 kHz, which are three to five orders of magnitude smaller than carrier frequencies in most of the over-water communication systems (100 MHz to 10 GHz). For example, a LoRa system at $f_c = 868$ MHz with BW = 500 kHz uses the frequency range from 867.75 MHz to 868.25 MHz. At a relative velocity of 30 m/s between transmitter and receiver (e. g., a car and a static gateway), the change in frequency ($f_y - f_x$, see Eq. (4)) is between 86.775 Hz and 86.825 Hz. The acoustic underwater FSCM transmission in [20] used $f_c = 62.5$ kHz with BW = 20 kHz (frequency is between 52.5 kHz and 72.5 kHz). A relative velocity of 1.5 m/s (e. g., a μAUV and a static sensor node) results in a frequency shift between 52.5 Hz and 72.5 Hz. Figure 2 illustrate the described difference between over-water and underwater communication. In the RF communication example, the frequency shift can be assumed as constant over the bandwidth (the difference is 0.05 Hz). Constant frequency shifts can be treated as CFO and removed with carrier frequency synchronization (see Section II-B). Opposed to that, the Doppler-introduced frequency shift increases 20 Hz over the frequency range for acoustic underwater communication and can not assumed as constant. In this case, it is not possible remove the Doppler effect with a carrier frequency synchronization and requires a dedicated algorithm to remove it.

In sum, the underwater acoustic transmission channel is a challenging transmission channel with multipath propagation, noise and massive Doppler shifts. Furthermore, the acoustic underwater channel changes frequently for example due to temperature variations, waves, different shipping activity, or tidal changes [68].

B. CHIRPS, FSCM AND NYQUIST RECEIVER

The following FSCM description is based on [2], [4], and [20]. The BB up-chirp, a linear complex up-chirp centered

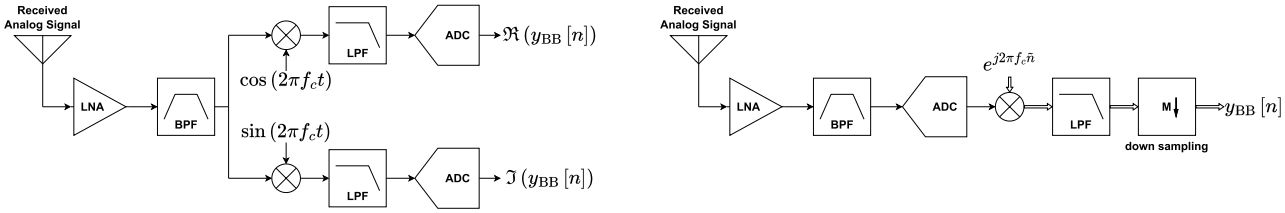

(a) Typical RF receiver structure.

(b) Typical acoustic underwater communication receiver structure.

FIGURE 5. Typical receiver structures for RF and acoustic underwater communication. Single line arrows indicate real-valued signals and double line arrows complex signals. Abbreviations: low-noise amplifier (LNA), band-pass filter (BPF), low-pass filter (LPF), analog-to-digital converter (ADC).

at 0 Hz is defined by

$$x_{\nearrow,\mathrm{BB}}(t) = e^{j2\pi \int_0^t f(\tau)\mathrm{d}\tau} = e^{j2\pi\left(\frac{\mu}{2}t - \frac{\mathrm{BW}}{2}\right)t} \tag{6}$$

with bandwidth BW, instantaneous frequency $f(t)$, chirp rate μ given by

$$\mu = \frac{\mathrm{d}f(t)}{\mathrm{d}t} = \frac{\mathrm{BW}}{T_{\mathrm{sym}}} \tag{7}$$

and symbol duration T_{sym}. Furthermore, the spreading factor SF is defined as

$$\mathrm{SF} = \log_2\left(T_{\mathrm{sym}}\mathrm{BW}\right) \;\Leftrightarrow\; 2^{\mathrm{SF}} = T_{\mathrm{sym}}\mathrm{BW}\,. \tag{8}$$

The spreading factor describes the relation of the number of bits per symbol and symbol duration for a constant bandwidth. Each symbol carries SF bits, which leads to 2^{SF} different data symbols. A Gray-coded data symbol $S \in \left\{0, 1, \ldots, 2^{\mathrm{SF}} - 1\right\}$ is modulated to a FSCM BB symbol $x_{S,\mathrm{BB}}(t)$ by [2]

$$x_{S,\mathrm{BB}}(t) = \begin{cases} e^{j2\pi\left(\frac{\mathrm{BW}}{2T_{\mathrm{sym}}}t^2 + \left(f(S) - \frac{\mathrm{BW}}{2}\right)t\right)}, & 0 \le t < t_{\mathrm{fold}} \\ e^{j2\pi\left(\frac{\mathrm{BW}}{2T_{\mathrm{sym}}}t^2 + \left(f(S) - \frac{3\mathrm{BW}}{2}\right)t\right)}, & t_{\mathrm{fold}} \le t < T_{\mathrm{sym}} \end{cases} \tag{9}$$

with the initial frequency $f(S) = S \cdot \frac{\mathrm{BW}}{2^{\mathrm{SF}}}$ and $t_{\mathrm{fold}} = \frac{2^{\mathrm{SF}} - S}{\mathrm{BW}}$.

To decode a received, sampled and synchronized symbol $y_{S,\mathrm{BB}}[n]$, a filter bank of 2^{SF} MFs can be applied. A computationally more efficient decoding method, called dechirping, is described in [2]. In short, the received symbol is sampled with sampling frequency BW resulting in 2^{SF} samples per symbol. Sampling with BW is called Nyquist sampling and allows to reconstruct frequencies in the range of $\pm\mathrm{BW}/2$. Afterwards, the discrete Fourier transform DFT $\{\cdot\}$ of the product of received BB symbol $y_{S,\mathrm{BB}}[n] \in \mathbb{C}^{2^{\mathrm{SF}}}$ and complex down chirp $x_{\searrow,\mathrm{BB}}[n] = \overline{x_{\nearrow,\mathrm{BB}}[n]} \in \mathbb{C}^{2^{\mathrm{SF}}}$ is computed by

$$\left[Y_0, Y_1, \ldots, Y_{2^{\mathrm{SF}}-1}\right] = \mathrm{DFT}\left\{y_{S,\mathrm{BB}}[n] \circ x_{\searrow,\mathrm{BB}}[n]\right\}\,. \tag{10}$$

Finally, a non-coherent detector estimates the data symbol with

$$\hat{S} = \underset{k}{\mathrm{argmax}}\left(|Y_k|\right). \tag{11}$$

C. SYMBOL OFFSETS

During the transmission and reception, different offsets have an effect on the received symbol. The offsets are illustrated in Fig. 4 and defined by:

- The symbol timing offset (STO) describes the difference in time, the delay τ, between the first estimate of the symbol boundaries and the real symbol boundaries.
- The carrier frequency offset (CFO) is the frequency difference γ between the carrier frequencies at transmitter and receiver.
- The sampling frequency offset (SFO) is the sampling frequency difference between transmitter and receiver. SFO and a motion introduced Doppler effect produce a scaling Δ in the time and frequency domain.

D. RECEIVER STRUCTURES

In many cases, the structure of underwater acoustic receivers are different to over-water RF receivers. A typical over-water RF receiver structure is depicted in Fig. 5a. The received analog signal, in this case the RF antenna output, is amplified with a low-noise amplifier (LNA) and filtered with a band-pass filter (BPF) to remove signal distortions outside the communication bandwidth. Afterwards, the received signal is shifted to the BB. The complex BB signal results from the multiplication with a sine and cosine oscillation with carrier frequency f_c and low-pass filter (LPF) filtering. At last, the in-phase and quadrature signals are sampled with analog-to-digital converters (ADCs) with BB sampling frequency $f_{s,\mathrm{BB}}$. $\Re(\cdot)$ and $\Im(\cdot)$ denote the real and imaginary part of a complex signal.

Opposed to that, typical acoustic underwater receivers, e. g., [21], [22], [50], and [51], sample the signal in the PB with sampling frequency $f_{s,\mathrm{PB}}$, after the received signal from the hydrophone passed a LNA and BPF. This receiver structure is typically used when $f_c \approx \mathrm{BW}$ and depicted in 5b. The shift from PB to BB can be implemented in software. In this case, the digital signal is multiplied with a complex oscillation and LPF filtered. At last, the signal is downsampled from $f_{s,\mathrm{PB}}$ to the BB sampling frequency $f_{s,\mathrm{BB}}$. Another option (for example implemented on the *ahoi* modem [21]) is a direct demodulation of the received PB signal without downshifting and downsampling.

Opposed to the first receiver structure (Fig. 5a), the second receiver (5b) prevents CFO due to the digital frequency shift.

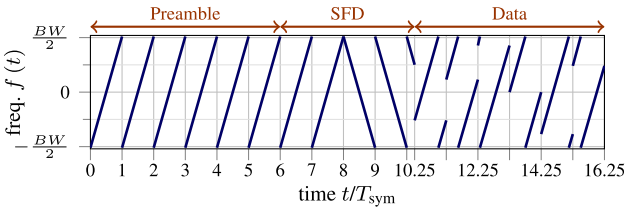

FIGURE 6. LoRa BB packet with preamble, starting frame delimiter (SFD) and six data symbols.

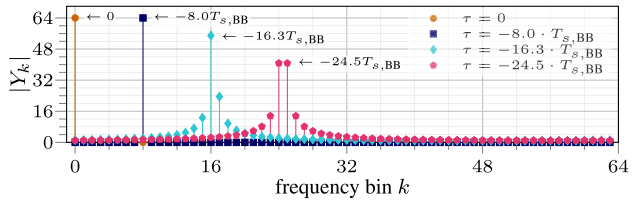

FIGURE 7. Effect of different symbol timing offset τ (STO) on the discrete Fourier transform (DFT) of the dechirped received signal with SF = 6, Nyquist sampling ($T_{s,\text{BB}}$ is the sampling interval) and non-coherent detection.

Furthermore, SFO effects the BB signal in the first case and the PB signal in the second case. To avoid confusions, passband sampling frequency offset (PB-SFO) and baseband sampling frequency offset (BB-SFO) are introduced to differentiate between both SFOs.

E. PACKET STRUCTURE

Figure 6 depicts a LoRa baseband packet with $N_{\text{pre}} = 6$ preamble symbols, $N_{\text{sfd}} = 4.25$ starting frame delimiter (SFD) symbols and $N_{\text{data}} = 6$ data symbols. The preamble consists of a sequence of up-chirps. The SFD of two up-chirps followed by 2.25 down-chirps. The two up-chirps of the SFD can be used as network identifier (see [7]) and modulated according to Eq. (9). In the following sections, the SFD starts with two unmodulated up-chirps. Preamble and SFD are used to detect a packet and to estimate STO, CFO, and SFO.

F. EFFECT OF SYMBOL TIMING OFFSET (STO)

To understand the effect of STO on chirping, a single received BB up-chirp is considered. Based on Eq. (6), a single received BB up-chirp $y_{\nearrow,\text{BB}}(t)$ with STO τ, where $0 \leq \tau \leq T_{\text{sym}}$, is

$$\begin{aligned} y_{\nearrow,\text{BB}}(t) &= x_{\nearrow,\text{BB}}(t-\tau) \\ &= e^{j2\pi\left(\frac{\text{BW}}{2T_{\text{sym}}}(t-\tau)-\frac{\text{BW}}{2}\right)(t-\tau)}. \end{aligned} \tag{12}$$

Afterwards, dechirping is applied on the received signal, resulting in the dechirped symbol $d(t)$ is defined by

$$\begin{aligned} d(t) &= y_{\nearrow,\text{BB}}(t) \cdot x_{\searrow,\text{BB}}(t) \\ &= e^{j2\pi\left(\frac{\text{BW}}{2T_{\text{sym}}}(t-\tau)-\frac{\text{BW}}{2}\right)(t-\tau)} \cdot e^{-j2\pi\left(\frac{\text{BW}}{2T_{\text{sym}}}t-\frac{\text{BW}}{2}\right)t} \\ &= e^{j2\pi\left(-\frac{\text{BW}}{T_{\text{sym}}}\tau t+\frac{\text{BW}}{2T_{\text{sym}}}\tau^2+\frac{\text{BW}}{2}\tau\right)}. \end{aligned} \tag{13}$$

By rearranging Eq. (13) the frequency and phase part of the dechirped symbol can be expressed as

$$d(t) = \underbrace{e^{-j2\pi\frac{\text{BW}}{T_{\text{sym}}}\tau t}}_{\text{frequency}} \cdot \underbrace{e^{j2\pi\left(\frac{\text{BW}}{2T_{\text{sym}}}\tau^2+\frac{\text{BW}}{2}\tau\right)}}_{\text{phase}}. \tag{14}$$

The STO changes the frequency of $d(t)$. Finally, the relation between the dechirped symbol's frequency $f_{\tau,\nearrow}$ and the STO τ can be obtained as

$$f_{\tau,\nearrow} = -\frac{\text{BW}}{T_{\text{sym}}} \cdot \tau \tag{15}$$

Comparable to Eq. (12), a single received BB down-chirp $y_{\searrow,\text{BB}}(t)$ with STO τ, $0 \leq \tau \leq T_{\text{sym}}$ is

$$\begin{aligned} y_{\searrow,\text{BB}}(t) &= x_{\searrow,\text{BB}}(t-\tau) \\ &= e^{-j2\pi\left(\frac{\text{BW}}{2T_{\text{sym}}}(t-\tau)-\frac{\text{BW}}{2}\right)(t-\tau)} \end{aligned} \tag{16}$$

The dechirped symbol $d(t)$ is defined by

$$\begin{aligned} d(t) &= y_{\searrow,\text{BB}}(t) \cdot x_{\nearrow,\text{BB}}(t) \\ &= \underbrace{e^{j2\pi\frac{\text{BW}}{T_{\text{sym}}}\tau t}}_{\text{frequency}} \cdot \underbrace{e^{-j2\pi\left(\frac{\text{BW}}{2T_{\text{sym}}}\tau^2+\frac{\text{BW}}{2}\tau\right)}}_{\text{phase}} \end{aligned} \tag{17}$$

The frequency $f_{\tau,\searrow}$ of $d(t)$ w. r. t. the STO τ is

$$f_{\tau,\searrow} = \frac{\text{BW}}{T_{\text{sym}}} \cdot \tau \tag{18}$$

The frequencies $f_{\tau,\nearrow}$ and $f_{\tau,\searrow}$ can be used to estimate the STO. Due to sampling, STO have an integer and fractional part. In the case of Nyquist sampling, the sampling interval is $T_{s,\text{BB}} = 1/f_{s,\text{BB}} = 1/\text{BW}$. Figure 7 shows the DFT of the sampled dechirped symbol $d(t)$ for different STOs τ in the middle of the preamble. That means the previous symbol (negative STO) and the following symbol (positive STO) is also an up-chirp. Without STO ($\tau = 0$), the peak of the DFT is the first bin, the constant component (origin direct current, DC) bin. In the second case, an integer STO of $\tau = -8.0 \cdot T_{s,\text{BB}}$ results in a single peak at bin 15. Opposed to that, the following STOs consist of an integer and fractional part ($\tau = -16.3 \cdot T_{s,\text{BB}}$ and $\tau = -24.5 \cdot T_{s,\text{BB}}$). The fractional STO distributes the energy over multiple DFT bin. In the worst case, the fractional part is half of the sampling interval. For $\tau = -24.5 \cdot T_{s,\text{BB}}$ the bins 24 and 25 have the same value. A simple peak detection based on Eq. (11) neglects the fractional part.

G. EFFECT OF DOPPLER SHIFT AND PB-SFO ON A SYMBOL

In the case of PB-sampling (c. f. receiver in Fig. 5b), Doppler shift and PB-SFO affect the received PB symbol in the same mode of operation. The received PB symbol $y_S(t)$ is defined based on the transmitted PB symbol $x_S(t)$

$$y_S(t) = x_S((1+\Delta)t) \tag{19}$$

with the time scaling factor

$$\Delta = \Delta_{\text{PB-SFO}} + \Delta_{\text{Doppler}}. \tag{20}$$

$\Delta_{\text{PB-SFO}}$ is the difference between sampling frequencies of transmitter and receiver. Δ_{Doppler} is introduced from a relative velocity v_0 between transmitter and receiver.

$$\Delta_{\text{Doppler}} = \frac{v_0}{c_{\text{sound}}} \quad \text{resp.} \quad \Delta_{\text{Doppler}} = \frac{v_0}{c_{\text{light}}} \tag{21}$$

TABLE 3. Doppler introduced frequency shifts of the dechirped symbol for different spreading factors SF with $f_c = 62.5\,\text{kHz}$ and $\text{BW} = 20.0\,\text{kHz}$. The Doppler shift is $\Delta = v_0/c_{\text{sound}} = 1.5\,\text{m/s}/1500\,\text{m/s} = 10^{-3}$. The last column depicts $f_{\Delta,\nearrow}$ in DFT bins (Nyquist sampling).

SF	T_{sym}	Bin Width	$f_{\Delta,\nearrow,\text{variable}}(t)$	$f_{\Delta,\nearrow,\text{const}}$	$f_{\Delta,\nearrow}$	$f_{\Delta,\nearrow}$
6	3.20 ms	312.50 Hz	max. 40.02 Hz	52.50 Hz	72.51 Hz	0.23
7	6.40 ms	156.25 Hz	max. 40.02 Hz	52.50 Hz	72.51 Hz	0.46
8	12.80 ms	78.13 Hz	max. 40.02 Hz	52.50 Hz	72.51 Hz	0.93
9	25.60 ms	39.06 Hz	max. 40.02 Hz	52.50 Hz	72.51 Hz	1.86
10	51.20 ms	19.53 Hz	max. 40.02 Hz	52.50 Hz	72.51 Hz	3.71

Usually $\Delta_{\text{Doppler}} \gg \Delta_{\text{PB-SFO}}$ and in the the remainder of this paper, the term *Doppler shift* includes PB-SFO.

Based on the BB up-chirp $x_{\nearrow,\text{BB}}(t)$, a transmitted PB up-chirp $x_{\nearrow}(t)$ at carrier frequency f_c is

$$\begin{aligned} x_{\nearrow}(t) &= \Re\left(x_{\nearrow,\text{BB}}(t)\cdot e^{j2\pi f_c t}\right) \\ &= \cos\left(2\pi\left(\frac{\text{BW}}{2T_{\text{sym}}}t - \frac{\text{BW}}{2} + f_c\right)t\right). \end{aligned} \tag{22}$$

The received PB up-chirp $y_{\nearrow}(t)$ with Doppler shift is according to Eq. (19):

$$\begin{aligned} y_{\nearrow}(t) &= x_{\nearrow}((1+\Delta)t) \\ &= \cos\left(2\pi\left(\frac{\text{BW}}{2T_{\text{sym}}}(1+\Delta)t - \frac{\text{BW}}{2} + f_c\right)(1+\Delta)t\right) \end{aligned} \tag{23}$$

The received PB up-chirp is shifted to the BB with an ideal low-pass filter $\text{LP}\{\cdot\}$.

$$\begin{aligned} y_{\nearrow,\text{BB}}(t) &= \text{LP}\left\{y_{\nearrow}(t)\cdot 2e^{-j2\pi f_c t}\right\} \\ &= e^{j2\pi\left(\frac{\text{BW}}{2T_{\text{sym}}}(1+\Delta)t - \frac{\text{BW}}{2}\right)(1+\Delta)t}\cdot e^{j2\pi f_c \Delta t} \end{aligned} \tag{24}$$

Afterwards, dechirping is applied.

$$\begin{aligned} d(t) &= y_{\nearrow,\text{BB}}(t)\cdot x_{\searrow,\text{BB}}(t) \\ &= e^{j2\pi\left(\frac{\text{BW}}{2T_{\text{sym}}}(1+\Delta)t - \frac{\text{BW}}{2}\right)(1+\Delta)t}\cdot e^{j2\pi f_c \Delta t} \\ &\quad\cdot e^{-j2\pi\left(\frac{\text{BW}}{2T_{\text{sym}}}t - \frac{\text{BW}}{2}\right)t} \end{aligned} \tag{25}$$

Equation (25) consists of a constant frequency and a variable time-dependent frequency:

$$d(t) = \underbrace{e^{j2\pi\left[\frac{\text{BW}}{2T_{\text{sym}}}(\Delta^2 t^2 + 2\Delta t^2)\right]}}_{\text{time dependent frequency}} \cdot \underbrace{e^{j2\pi\left[f_c\Delta t - \frac{\text{BW}}{2}\Delta t\right]}}_{\text{constant frequency}} \tag{26}$$

The constant frequency $f_{\Delta,\nearrow,\text{const}}$ is

$$\begin{aligned} f_{\Delta,\nearrow,\text{const}} &= \frac{\text{d}}{\text{d}t}\left[f_c\Delta t - \frac{\text{BW}}{2}\Delta t\right] \\ &= \left(f_c - \frac{\text{BW}}{2}\right)\Delta \end{aligned} \tag{27}$$

and the time-dependent frequency $f_{\Delta,\nearrow,\text{variable}}(t)$ is

$$\begin{aligned} f_{\Delta,\nearrow,\text{variable}}(t) &= \frac{\text{d}}{\text{d}t}\left[\frac{\text{BW}}{2T_{\text{sym}}}\left(\Delta^2 t^2 + 2\Delta t^2\right)\right] \\ &= \frac{\text{BW}}{T_{\text{sym}}}\left(\Delta^2 t + 2\Delta t\right). \end{aligned} \tag{28}$$

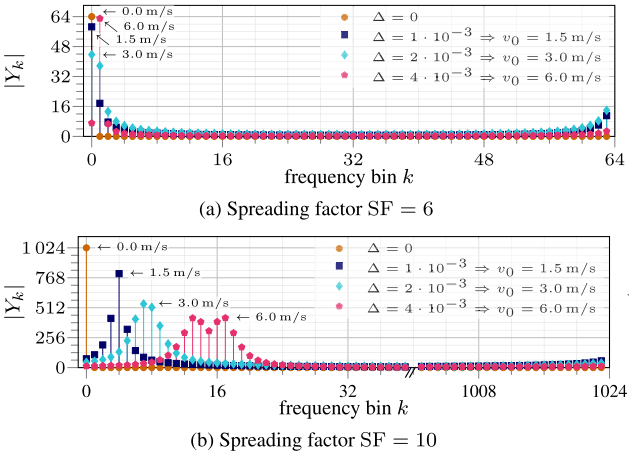

(a) Spreading factor SF = 6

(b) Spreading factor SF = 10

FIGURE 8. Effect of Doppler shifts on the DFT of the dechirped symbol for $\text{SF} \in \{6, 10\}$. In all cases the transmitted symbols is an up-chirp at carrier frequency $f_c = 62.5\,\text{kHz}$ and $\text{BW} = 20.0\,\text{kHz}$ bandwidth. The speed of sound is $c_{\text{sound}} = 1500\,\text{m/s}$.

For $t \in [0, T_{\text{sym}}]$ the time-dependent frequency increases linear from $f_{\Delta,\nearrow,\text{variable}}(0) = 0$ to

$$\begin{aligned} f_{\Delta,\nearrow,\text{variable}}(T_{\text{sym}}) &= \frac{\text{BW}}{T_{\text{sym}}}\left(\Delta^2 T_{\text{sym}} + 2\Delta T_{\text{sym}}\right) \\ &= \text{BW}\left(\Delta^2 + 2\Delta\right) \end{aligned} \tag{29}$$

The average frequency shift is

$$\begin{aligned} f_{\Delta,\nearrow} &= \frac{f_{\Delta,\nearrow,\text{variable}}(T_{\text{sym}})}{2} + f_{\Delta,\nearrow,\text{const}} \\ &= \left(f_c + \frac{\text{BW}}{2}(1+\Delta)\right)\Delta \end{aligned} \tag{30}$$

Similar calculations can be used to identify the effect to a received down-chirp. The dechirped signal of a received down-chirp is

$$d(t) = \underbrace{e^{j2\pi\left[-\frac{\text{BW}}{2T_{\text{sym}}}(\Delta^2 t^2 + 2\Delta t^2)\right]}}_{\text{time dependent frequency}} \cdot \underbrace{e^{j2\pi\left[f_c\Delta t + \frac{\text{BW}}{2}\Delta t\right]}}_{\text{constant frequency}} \tag{31}$$

The constant frequency $f_{\Delta,\searrow,\text{const}}$ is

$$f_{\Delta,\searrow,\text{const}} = \left(f_c + \frac{\text{BW}}{2}\right)\Delta \tag{32}$$

and the time-dependent frequency $f_{\Delta,\searrow,\text{variable}}(t)$ is

$$f_{\Delta,\searrow,\text{variable}}(t) = -\frac{\text{BW}}{T_{\text{sym}}}\left(\Delta^2 t + 2\Delta t\right). \tag{33}$$

Finally, the average frequency shift for a down-chirp is

$$f_{\Delta,\searrow} = \left(f_c - \frac{\text{BW}}{2}(1+\Delta)\right)\Delta. \tag{34}$$

The effect of Doppler shifts depend on the communication system. For example, in RF-based over-water communication $f_c \gg \text{BW}$. In this case, Eqs. (30), and (34) can be simplified to $f_{\Delta,\nearrow} \approx f_{\Delta,\searrow} \approx f_c\Delta$. This simplification is used for example in [29]. On the other hand, Doppler shifts added

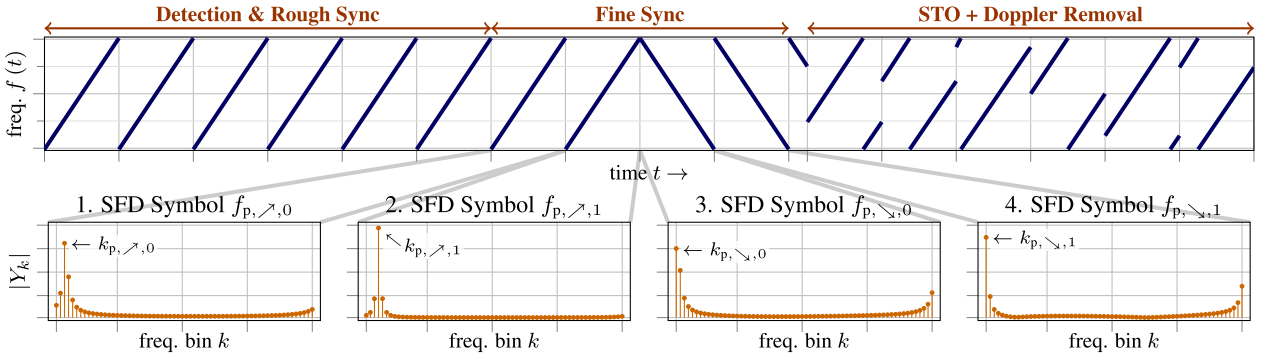

FIGURE 9. Processing steps of the proposed receiver structure. The preamble is used for detection and rough synchronization. The two up-chirps and two down-chirps of the SFD for a fine synchronization (estimation of STO and Doppler shift). Afterwards STO and Doppler shift are removed in the modulated data symbols. The second row depicts the peak detection of the SFD.

a time-dependent frequency shift to the dechirped signal (c. f. Eqs. (28), and (33)). The time-dependent frequency shift spreads the energy for large Doppler shifts over multiple frequency bins in the DFT. In acoustic underwater communication typically $f_c \approx \mathrm{BW}$. Therefore the bandwidth plays an important aspect in Eqs. (30), and (34). Table (3) depicts examples for different spreading factors SF. The carrier frequency $f_c = 62.5\,\mathrm{kHz}$ and bandwidth $\mathrm{BW} = 20.0\,\mathrm{kHz}$ are identical to the setup in [20]. The frequencies $f_{\Delta,\nearrow,\mathrm{variable}}(t)$, $f_{\Delta,\nearrow,\mathrm{const}}$, and $f_{\Delta,\nearrow}$ correspond to a Doppler shift of $\Delta = v_0/c_{\mathrm{sound}} = 1.5\,\mathrm{m/s}/1500\,\mathrm{m/s} = 10^{-3}$. The time-dependent frequency shift $f_{\Delta,\nearrow,\mathrm{variable}}(t) \in [0\,\mathrm{Hz}, 40\,\mathrm{Hz}]$ and the average frequency shift $f_{\Delta,\nearrow} = 72.5\,\mathrm{Hz}$ are independent of SF. Indeed, the DFT bin width (Nyquist sampling) depends on SF. For $\mathrm{SF} = 6$ the DFT bin width is 312.50 Hz and larger than $f_{\Delta,\nearrow,\mathrm{variable}}(t)$ and $f_{\Delta,\nearrow}$. Larger spreading factors result in smaller DFT bin width. In the case of $\mathrm{SF} = 10$ the bin width is 19.53 Hz. Hence, the time-dependent frequency shift spreads the energy over multiple bins. Furthermore, the average frequency shift $f_{\Delta,\nearrow}$ shifts the peak 3.71 samples in the DFT of the dechirped symbol.

Therefore, smaller spreading factors are more resilient against Doppler shifts. Figure 8 shows the DFT results for $\mathrm{SF} = 6$ and $\mathrm{SF} = 10$ for different Doppler shifts $\Delta \in \{0, 10^{-3}, 2 \cdot 10^{-3}, 4 \cdot 10^{-3}\}$, which correspond to $v_0 \in \{0, 1.5\,\mathrm{m/s}, 3.0\,\mathrm{m/s}, 6.0\,\mathrm{m/s}\}$ at a speed of sound $c_{\mathrm{sound}} = 1500\,\mathrm{m/s}$. For $\mathrm{SF} = 6$ (c. f. Fig. 8a), Doppler shifts have a minor effect. A shift of $\Delta = 10^{-3}$ lowers the energy peak slightly compared to the static scenario ($\Delta = 0$). A shift of $\Delta = 2 \cdot 10^{-3}$ splits the energy into the two bins 0 and 1. Finally, a shift of $\Delta = 4 \cdot 10^{-3}$ results in a strong peak at bin 1. Opposed to that, Doppler shifts have a strong effect for $\mathrm{SF} = 10$ (c. f. Fig. 8b). In all cases, the number of shifted bins is higher (due to a smaller bin width) and the result of the time-dependent frequency shift $f_{\Delta,\nearrow,\mathrm{variable}}(t)$ (c. f. Eq. (28)) gets visible. For Example for $\Delta = 4 \cdot 10^{-3}$ the energy is spread over the range $f_{\Delta,\nearrow,\mathrm{variable}}(t) \in [0\,\mathrm{Hz}, 160.3\,\mathrm{Hz}]$ which belongs to 8.2 DFT bins (c. f. Table 3). The peak for $\Delta = 4 \cdot 10^{-3}$ in Fig. 8b is circa 8 samples wider than the peak in without Doppler shift ($\Delta = 0$). The energy stays similar, which means a wider peaks results in a lower peak height and therefore a lower peak to noise ratio.

H. EFFECT OF DOPPLER SHIFT ON A PACKET

In addition to the previously discussed effect of Doppler shifts on a single symbol (c. f. Section III-G), Doppler shifts produce an increasing or decreasing STO over time (c. f. Eq. (19)). For example, if the first symbol is perfectly synchronized, the following symbol has an additional STO of

$$\tau_{\Delta,T_{\mathrm{sym}}} = -T_{\mathrm{sym}} \cdot \Delta \tag{35}$$

Based on Eqs. (15), and (18), this results in additional frequency shifts of

$$f_{\tau_{\Delta,T_{\mathrm{sym}}},\nearrow} = -\frac{\mathrm{BW}}{T_{\mathrm{sym}}} \cdot \tau_{\Delta,\mathrm{symb}} = \mathrm{BW} \cdot \Delta \tag{36}$$

$$f_{\tau_{\Delta,T_{\mathrm{sym}}},\searrow} = -\mathrm{BW} \cdot \Delta \tag{37}$$

in the DFT of the dechirped symbol for an up or down-chirp. Table 4 illustrates the time shift per symbol. The setup is similar to Table 3. A higher spreading SF results in a longer symbol duration and therefore higher time and frequency shifts. In the case of $\mathrm{SF} = 10$, the shift is a single sample per symbol and results in symbol detection errors (c. f. Eq. (11)).

TABLE 4. Doppler introduced time shifts (c. f. Eq. (35)) after a single symbol for different spreading factors SF with $\mathrm{BW} = 20.0\,\mathrm{kHz}$. The Doppler shift is $\Delta = v_0/c_{\mathrm{sound}} = 1.5\,\mathrm{m/s}/1500\,\mathrm{m/s} = 10^{-3}$. The sampling interval is 1/BW. The last column depicts $f_{\tau_{\Delta,T_{\mathrm{sym}}}}$ in DFT bins.

SF	T_{sym}	Bin Width	1/BW	$\tau_{\Delta,T_{\mathrm{sym}}}$	$f_{\tau_{\Delta,T_{\mathrm{sym}}}}$	$f_{\tau_{\Delta,T_{\mathrm{sym}}}}$
6	3.20 ms	312.50 Hz	50 µs	−3.20 µs	±20 Hz	±0.06
7	6.40 ms	156.25 Hz	50 µs	−6.40 µs	±20 Hz	±0.13
8	12.80 ms	78.13 Hz	50 µs	−12.80 µs	±20 Hz	±0.26
9	25.60 ms	39.06 Hz	50 µs	−25.60 µs	±20 Hz	±0.51
10	51.20 ms	19.53 Hz	50 µs	−51.20 µs	±20 Hz	±1.02

IV. DOPPLER SHIFT ROBUST RECEIVER IMPLEMENTATION

Next, we describe the proposed and implemented receiver structure. The reception of an acoustic FSCM packet (c. f. Fig. 9) passes through the following steps:

1) Packet detection and rough STO estimation based on the preamble symbols (Section IV-A)
2) Doppler shift (and PB-SFO) and STO estimation with the SFD symbols (Section IV-B, IV-C)
3) Removal or compensation of all offsets (Section IV-D)
4) Data symbol decoding (Section IV-E)

A. PREAMBLE DETECTION

The synchronization starts with the preamble detection. Typically, the received signal is processed in blocks of 2^{SF} samples and dechirping (Eq. (10)) is applied. If the energy of the maximum DFT value (Eq. (11)) exceeds a threshold, a preamble symbol is detected. Usually two or more preamble symbols are used to avoid false detection. For example Ghanaatian et al. [2] expect $N_{\mathrm{pre}} - 1$ with equal maximum bin index for preamble detection. Tapparel et al. [32] added a margin of ± 1 sample to this condition to enhance the robustness against demodulation errors in the case of additional noise. Bernier et al. [5] discussed an averaging of multiple blocks of DFT magnitudes to cancel out noise. In their implementation they used a block-wise infinite impulse response (IIR) filter instead of averaging for a more lightweight implementation.

The Doppler effect shifts the peak over the time (see Section III-H). Based on that, averaging, IIR filtering or peak detection at similar bins are not applicable. Our preamble detection algorithm works as follows: If the energy of a DFT bin exceeds a threshold, an up-chirp is assumed. The threshold is a multiple of the average magnitude DFT. The threshold has to be selected in order that the probability of a false detection P_{fa} is minimized and the probability of detection P_{d} is maximized. In Section V-A thresholds are selected based on a simulation study. It is important to note, that fractional STOs and Doppler shifts lower the maximum peak (c. f. Figs. 7 and (8)) and therefore a lower threshold is required for correct detection in these cases. After the detection of the first preamble symbol, the following blocks are re-aligned according to Eq. 15. Afterwards each block contains a symbol. The following symbols have to exceed the threshold and the maximum peak position k_{p} must be inside the range k_{diff}

$$k_{\mathrm{diff}} = \left\lceil |\Delta_{\max}| \cdot 2^{\mathrm{SF}} \cdot \left(N_{\mathrm{pre}} + N_{\mathrm{sfd}}\right) \right\rceil \tag{38}$$

which means

$$0 \leq k_{\mathrm{p}} \leq k_{\mathrm{diff}} \quad \text{or} \quad 2^{\mathrm{SF}} - k_{\mathrm{diff}} \leq k_{\mathrm{p}} \leq 2^{\mathrm{SF}} - 1 \tag{39}$$

with the maximal expected absolute Doppler Shift $|\Delta_{\max}|$ and the ceiling operator $\lceil \cdot \rceil$. If the peak of the following symbol is below the threshold or outside the range k_{diff} the preamble detection is aborted. Equations. (38), and (39) include the behavior that the Doppler effect stretches or compresses the signal over time (c. f. Section (III-H)). At least, one preamble symbol for re-alignment is required before the SFD (the SFD symbols have to exceed the threshold too). This triggers a re-synchronization in the case of failures during the preamble detection.

B. STO AND DOPPLER SHIFT ESTIMATION

First, the preamble is used to compensate a rough integer STO estimation. Afterwards, a SFD of two up-chirps and two down-chirps is used for fine STO and Doppler Shift calculation. After dechirping and peak detection, the four frequencies $f_{\mathrm{p},\nearrow,0}$, $f_{\mathrm{p},\nearrow,1}$, $f_{\mathrm{p},\searrow,0}$, $f_{\mathrm{p},\searrow,1}$ correspond to the frequency peaks of the four dechirped SFD symbols. Figure 10 shows the DFT transformed dechirping results of the four SFD symbols.

To increase the accuracy, the peak frequency f_{p} of a DFT is calculated with the frequency estimator from [40] (comparable to Xhonneux et al. [7]).

$$f_{\mathrm{p}} = \left(k_{\mathrm{p}} + \frac{\left|Y_{k_{\mathrm{p}}+1}\right| - \left|Y_{k_{\mathrm{p}}-1}\right|}{4\left|Y_{k_{\mathrm{p}}}\right| - 2\left|Y_{k_{\mathrm{p}}+1}\right| - 2\left|Y_{k_{\mathrm{p}}-1}\right|} \right) \cdot \frac{\mathrm{BW}}{2^{\mathrm{SF}}} \tag{40}$$

or

$$f_{\mathrm{p}} = \left(k_{\mathrm{p}} - \Re\left(\frac{Y_{k_{\mathrm{p}}+1} - Y_{k_{\mathrm{p}}-1}}{2Y_{k_{\mathrm{p}}} - Y_{k_{\mathrm{p}}+1} - Y_{k_{\mathrm{p}}-1}} \right) \right) \cdot \frac{\mathrm{BW}}{2^{\mathrm{SF}}} \tag{41}$$

with the frequency bin index $k_{\mathrm{p}} \in \left\{0, 1, \ldots, 2^{\mathrm{SF}} - 1\right\}$ of the highest DFT magnitude sample $\left|Y_{k_{\mathrm{p}}}\right|$ and the neighbor complex samples $Y_{k_{\mathrm{p}}+1}$ and $Y_{k_{\mathrm{p}}-1}$. Equation (40) uses magnitude values (similar to the non-coherent detection), but Eq. (41) is more robust against noise [40]. Equation. (41) is used for the detection of the SFD peaks.

Afterwards, the four frequency peaks are used to construct the following equation system.

$$\begin{aligned} f_{\mathrm{p},\nearrow,0} &= f_{\Delta,\nearrow} + f_{\tau,\nearrow} \\ &= \left(f_c + \frac{\mathrm{BW}}{2} + \frac{\mathrm{BW}}{2}\Delta \right) \Delta - \frac{\mathrm{BW}}{T_{\mathrm{sym}}}\tau \end{aligned} \tag{42}$$

$$\begin{aligned} f_{\mathrm{p},\nearrow,1} &= f_{\Delta,\nearrow} + f_{\tau,\nearrow} + f_{\tau_{\Delta,T_{\mathrm{sym}}},\nearrow} \\ &= \left(f_c + \frac{3\mathrm{BW}}{2} + \frac{\mathrm{BW}}{2}\Delta \right) \Delta - \frac{\mathrm{BW}}{T_{\mathrm{sym}}}\tau \end{aligned} \tag{43}$$

$$\begin{aligned} f_{\mathrm{p},\searrow,0} &= f_{\Delta,\searrow} + f_{\tau,\searrow} + 2 \cdot f_{\tau_{\Delta,T_{\mathrm{sym}}},\searrow} \\ &= \left(f_c - \frac{5\mathrm{BW}}{2} - \frac{\mathrm{BW}}{2}\Delta \right) \Delta + \frac{\mathrm{BW}}{T_{\mathrm{sym}}}\tau \end{aligned} \tag{44}$$

$$\begin{aligned} f_{\mathrm{p},\searrow,1} &= f_{\Delta,\searrow} + f_{\tau,\searrow} + 3 \cdot f_{\tau_{\Delta,T_{\mathrm{sym}}},\searrow} \\ &= \left(f_c - \frac{7\mathrm{BW}}{2} - \frac{\mathrm{BW}}{2}\Delta \right) \Delta + \frac{\mathrm{BW}}{T_{\mathrm{sym}}}\tau \end{aligned} \tag{45}$$

The STO is defined w. r. t. the begin of the first up-chirp. Under the assumption $1 \gg \Delta$ the system can be simplified

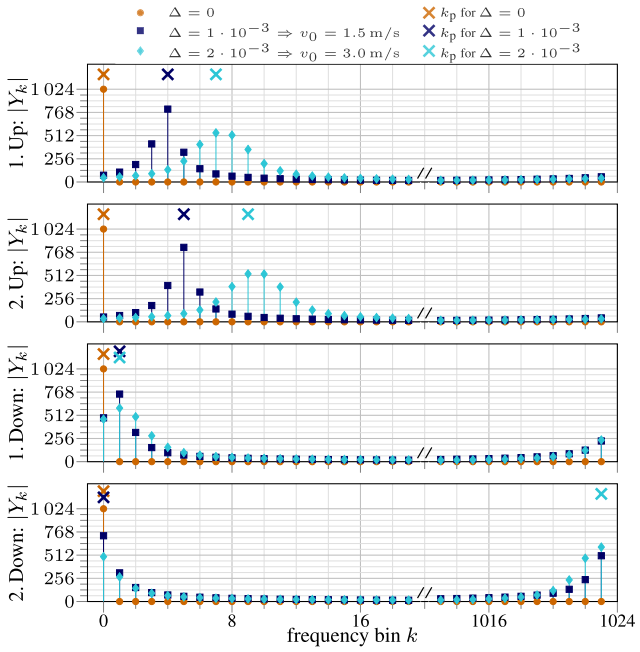

FIGURE 10. DFT results of the dechirped SFD symbols with SF = 10, f_c = 62.5 kHz, and BW = 20.0 kHz for different Doppler shifts. The speed of sound is c_{sound} = 1500 m/s. The crosses indicate the frequency index k_p with the highest magnitude (c. f. Eqs. (40), and (41)).

and rearranged to a linear equation system.

$$\underbrace{\begin{pmatrix} f_{\text{p},\nearrow,0} \\ f_{\text{p},\nearrow,1} \\ f_{\text{p},\searrow,0} \\ f_{\text{p},\searrow,1} \end{pmatrix}}_{b} = \underbrace{\begin{pmatrix} f_c + \frac{\text{BW}}{2} & -\frac{\text{BW}}{T_{\text{sym}}} \\ f_c + \frac{3\text{BW}}{2} & -\frac{\text{BW}}{T_{\text{sym}}} \\ f_c - \frac{5\text{BW}}{2} & \frac{\text{BW}}{T_{\text{sym}}} \\ f_c - \frac{7\text{BW}}{2} & \frac{\text{BW}}{T_{\text{sym}}} \end{pmatrix}}_{A} \cdot \underbrace{\begin{pmatrix} \Delta \\ \tau \end{pmatrix}}_{x} \tag{46}$$

Finally, the system can be solved with linear least squares (LLS) [69, Ch. 2]

$$\hat{x} = \left(A^T A\right)^{-1} A^T b \tag{47}$$

where $\hat{x}$ is a vector with the estimates of Δ and τ. It is important to note, that there exist computational more stable methods to solve Eq. (46). On the other hand, Eq. (47) is simple to implement on a microcontroller for a 4×2 matrix.

C. REFERENCE IMPLEMENTATION

To compare the new algorithm from Section IV-B, a modified implementation of the up-down method from Diamant et al. [44] (c. f. Section II-C) is applied. Diamant et al. used the properties of the MF with an up or down-chirp. A positive Doppler shift results in a negative shift of the lag in the case of an up-chirp and a positive shift for a down-chirp. Negative Doppler shifts have the inverse behavior. Based on the difference between the MF peaks the Doppler shift can be estimated. It is important to note, that the implementation of a MF requires higher computational resources compared to dechirping. To dechirp a symbol with 2^{SF} samples, a single DFT of size 2^{SF} is required. Opposed to that, a matched filter with negative and positive lag, requires three DFTs of size $2^{\text{SF}+1}$ [69, Ch. 13]. The DFT of the reference symbol is not required for every symbol. In an efficient implementation, a matched filter requires two DFTs of size $2^{\text{SF}+1}$.

Opposed to Diamant et al., the modified algorithm includes the two up-chirps and down-chirps of the SFD. The lags $\tau_{\text{p},\nearrow,0}$, $\tau_{\text{p},\nearrow,1}$, $\tau_{\text{p},\searrow,0}$, and $\tau_{\text{p},\searrow,1}$ are the lags with the highest matched filter result. Based on the lags, the Doppler shift is calculated from

$$\Delta = -\frac{1}{2}\left(\frac{-f_c}{\text{BW}} + 1 - \frac{\delta}{2T_{\text{sym}}}\right) \pm \sqrt{\frac{\left(\frac{-f_c}{\text{BW}} + 1 - \frac{\delta}{2T_{\text{sym}}}\right)^2}{4} + \frac{\delta}{2T_{\text{sym}}}} \tag{48}$$

with

$$\delta = \frac{\tau_{\text{p},\nearrow,0} + \tau_{\text{p},\nearrow,1} - \tau_{\text{p},\searrow,0} - \tau_{\text{p},\searrow,1}}{2}. \tag{49}$$

The entire derivations of the equations are included in the appendix. Afterwards, the Doppler shift is removed to get $\hat{\tau}_{\text{p}}$ from τ_{p}. Finally, the STO is the mean of the Doppler shift corrected peak lags:

$$\tau = \frac{\hat{\tau}_{\text{p},\nearrow,0} + \hat{\tau}_{\text{p},\nearrow,1} + \hat{\tau}_{\text{p},\searrow,0} + \hat{\tau}_{\text{p},\searrow,1}}{4} \tag{50}$$

D. STO AND DOPPLER SHIFT REMOVAL

After the estimation of STO and Doppler shifts, the offsets must be removed for an error-free symbol demodulation. The proposed acoustic underwater receiver samples the PB signal. Afterwards, the signal is shifted and sampled-down in software (c. f. Section III-D). The offsets are removed in the PB. In the case of STO only, similar methods can be applied in the BB signal (in the best case before down-sampling). Doppler shifts can be removed by reversing the effect of Eq. (19). The Doppler shift free signal $\widehat{y_S}(t)$ of $y_S(t)$ is:

$$\widehat{y_S}(t) = y_S((1 - \Delta)t) \tag{51}$$

Four different strategies are implemented: (1) Removal of integer STO only. (2) Linear interpolation to remove STO. (3) Linear interpolation to remove STO and Doppler shifts. (4) Nearest PB sample to remove STO and Doppler shifts. Ghanaatian et al. [2] suggested an over-sampling of the BB to remove BB-SFO. The selection of the nearest sample in the PB is an adaption of this algorithm and takes advantage of the different structure of acoustic underwater receivers. In this case, the nearest time sample in the PB is selected instead of interpolation. Compared to interpolation, this method is less computational expensive.

E. DIFFERENTIAL CODING AND DECODING

Ben Temim et al. [31] used a differential symbol coding to compensate CFO and Rezzouki et al. [33] implemented a differential symbol coding for acoustic underwater communication. We use a normal symbol demodulation (according

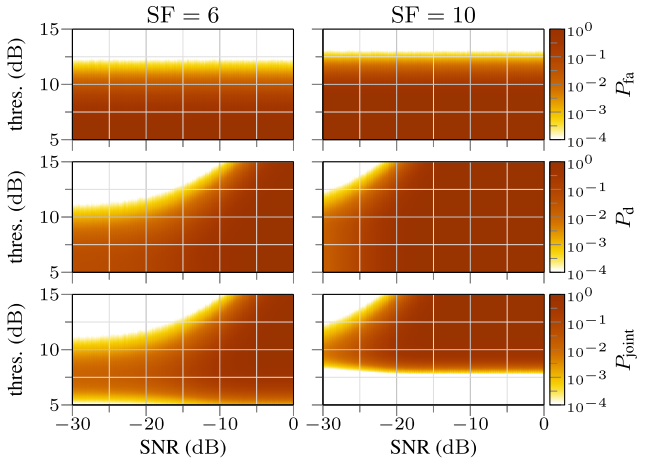

FIGURE 11. Simulation results for different preamble detection thresholds. The diagrams show the false detection probability P_{fa}, detection probability P_d and the joint probability P_{joint}.

to Eq. (11)) and a differential symbol coding. For the demodulation of differential symbols two different approaches are compared. In the first case and similar to Ben Temim et al., the received differential symbols are estimated with Eq. (11) and the difference on the integer level is the demodulated symbol. This method is called *differential binary* symbol decoding in the following sections. We developed a novel method, called *differential peak* symbol decoding, which uses the estimated frequency peaks (c. f. Eq. 40) from the current differential symbol $f_{\mathrm{p,n}}$ and previous differential symbol $f_{\mathrm{p,n\text{-}1}}$. The estimated data symbol is:

$$\hat{S} = \mathrm{round}\left[\left(f_{\mathrm{p,n}} - f_{\mathrm{p,n\text{-}1}}\right) \cdot \frac{2^{\mathrm{SF}}}{\mathrm{BW}}\right] \bmod 2^{\mathrm{SF}} \tag{52}$$

F. DIFFERENT SPREADING FACTORS FOR SYNCHRONIZATION AND DATA TRANSMISSION

Section III-G derived that symbols with a lower spreading SF have an higher resilience against Doppler shifts. On the other hand, symbols with higher spreading factors are more effected by Doppler shift and therefore suitable for Doppler shift estimation. Hence, symbols with higher spreading can be used for the preamble and SFD and a lower spreading for data transmission. This enables a proper estimation and compensation of STO and Doppler shift and a high resilience against Doppler shifts of the transmitted data symbols.

V. EVALUATION AND DISCUSSION

This section examines and discusses the results of the implemented algorithms from Section IV. The algorithms were implemented with MATLAB and are public available.[2] First, the preamble detection threshold was determined and the accuracy of our joint estimation of STO and Doppler shift was evaluated. Afterwards, the BER for different spreading, packet length, removal techniques, and symbol coding were compared. In this paper, the acoustic underwater transmission channel is simplified to a single propagation path, with additional noise, propagation time delays, and Doppler shifts. The simplification to a single propagation path with additional noise is similar to most of the in Section II-B discussed research papers [2], [5], [6], [7], [31], [32].

In all simulations, a PB sampling rate $f_{s,\mathrm{PB}} = 200\,\mathrm{kHz}$ and a carrier frequency $f_c = 62.5\,\mathrm{kHz}$ was selected similar to the sampling frequency and carrier frequency of the *ahoi* modem [21]. The bandwidth was set to $\mathrm{BW} = 20\,\mathrm{kHz}$ and accordingly the BB sampling rate to $f_{s,\mathrm{BB}} = 20\,\mathrm{kHz}$. Spreading factors of $\mathrm{SF} \in \{6, 10\}$ were used. The bandwidth and spreading factors were similar to [20] and resulted in symbol lengths of $T_{\mathrm{sym}} \in \{3.2\,\mathrm{ms}, 51.2\,\mathrm{ms}\}$. The BER was measured without additional error correcting code to evaluate the direct impact on the symbol demodulation. Gray mapping was used for symbol generation (c. f. Section III-B). The signal-to-noise ratio (SNR) was always measured over the PB communication bandwidth $[f_c - \mathrm{BW}/2, f_c + \mathrm{BW}/2] = [52.5\,\mathrm{kHz}, 72.5\,\mathrm{kHz}]$ and the speed of sound was set to $c_{\mathrm{sound}} = 1500\,\mathrm{m/s}$.

A. PREAMBLE DETECTION

The packet reception started with the preamble detection based on a threshold (c. f. Section IV-A). The threshold was defined as the difference between the average over the DFT magnitudes and the minimum peak high for detection. The selected threshold had to minimize the probability of a false detection P_{fa} and maximize the probability of detection P_{d}. Furthermore, the joint probability was defined

$$P_{\mathrm{joint}} = (1 - P_{\mathrm{fa}}) \cdot P_{\mathrm{d}}. \tag{53}$$

During the simulation, SNRs between $-30\,\mathrm{dB}$ to $0\,\mathrm{dB}$ and threshold factors from 5 dB to 15 dB were simulated without velocity. Noise was generated according to the SNR. If the maximum magnitude of the dechirped noise was above the threshold, P_{fa} increased. If the symbol with additional noise was detected, P_{d} increased. For every SNR and threshold, 10^6 repetitions with a randomly selected fractional STO between ± 0.5 BB sample were simulated.

The simulation results are depicted in Fig. 11. Based on the simulations, the thresholds factors 11 dB (SF = 6) and 12 dB (SF = 10) were selected for the following evaluation. The false detection probability was $P_{\mathrm{fa}} = 3.2 \times 10^{-3}$ respectively $P_{\mathrm{fa}} = 4.0 \times 10^{-3}$ and the detection probability of $P_{\mathrm{d}} = 1$ was achieved above 0.25 dB respectively $-12.75\,\mathrm{dB}$.

B. STO AND DOPPLER SHIFT ESTIMATION

To evaluate the STO and Doppler shift estimator, a simulation with STOs from -100 to 100 PB samples with 1 sample resolution (-10 to 10 BB samples with 0.1 sample resolution), velocities from $-6\,\mathrm{m/s}$ to $6\,\mathrm{m/s}$ with $0.1\,\mathrm{m/s}$ resolution (Doppler shifts from -4×10^{-3} to 4×10^{3}) and SNR from $-15\,\mathrm{dB}$ to $15\,\mathrm{dB}$ with $1\,\mathrm{dB}$ resolution were carried

[2] https://collaborating.tuhh.de/e-24/public/underwater/fscm-doppler-receiver/

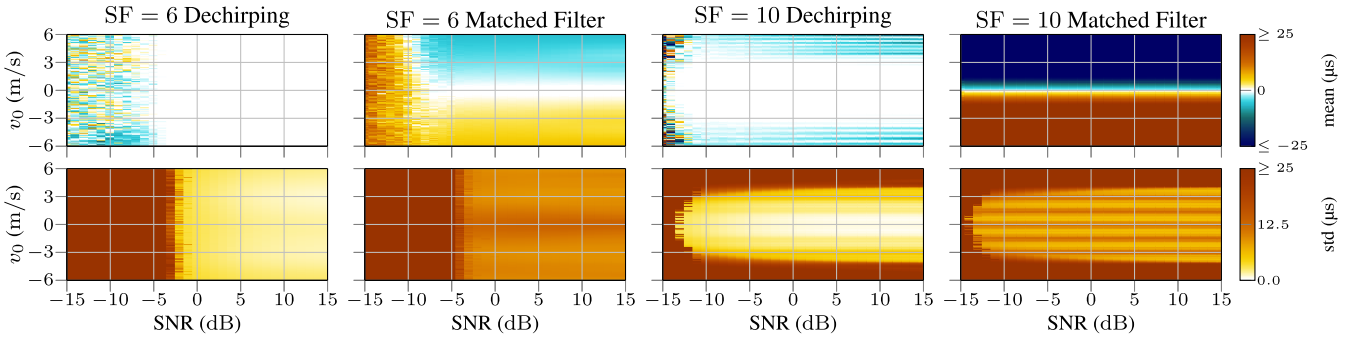

FIGURE 12. Simulation results (mean error and standard deviation) for STO estimation. Our algorithm from Section IV-B is titled with *dechirping* and the reference implementation (c. f. Section IV-C) with *matched filter*. A STO of ±25 µs (minimum and maximum values) is ±0.5 BB sample.

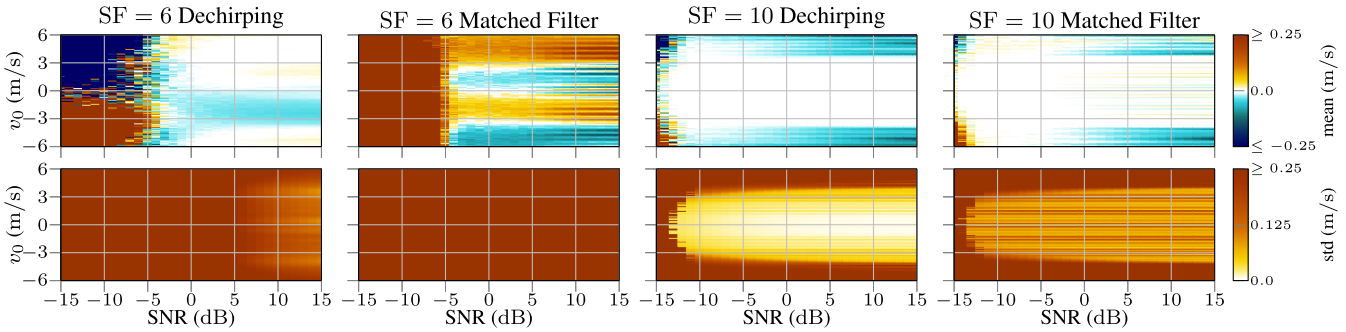

FIGURE 13. Simulation results (mean error and standard deviation) for Doppler shift estimation. Our algorithm from Section IV-B is titled with *dechirping* and the reference implementation (c. f. Section IV-C) with *matched filter*. A velocity of ±0.25 m/s (minimum and maximum values) results in a Doppler shift of $\Delta = \pm 1/6 \times 10^{-3}$.

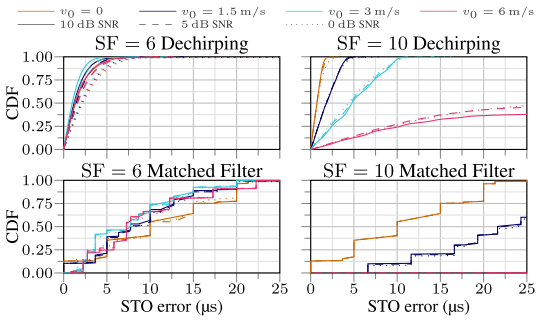

FIGURE 14. CDF of the symbol timing offset (STO) estimation error. *Dechirping* corresponds to the algorithm in Section IV-B, *matched filter* to Section IV-C.

out. Each constellation point, the simulation was repeated 100 times with different randomly generated noise. In sum, the simulation ran 7.5×10^7 iterations per spreading factor. The results for the joint estimator (Section IV-B) and the reference implementation (Section IV-C) is shown in Fig. 12, 13.

First, in Fig. 12 the STO is plotted with mean error value and standard deviation of the estimation algorithms. For both spreading factors, our algorithm from Section IV-B had a lower mean error and standard deviation compared to the reference implementation from Section IV-C. A lower spreading factor required higher SNR for comparable errors. In the case of a spreading factor of SF = 10, the mean error and standard deviation increased for absolute velocities above 3 m/s. This support the results from Section III-G, that a lower spreading factor is more resilient against Doppler shifts.

Similar to Fig. 12, Fig. 13 shows the results of the velocity estimation. Our algorithm has a better accuracy compared to the reference algorithm. However, the results for SF = 6 showed a high variance compared to SF = 10, which means that a higher spreading factor leads to a more precise velocity estimation. For a comparison, the cumulative distribution functions (CDFs) for different velocities of $v_0 = \{0\,\text{m/s}, 1.5\,\text{m/s}, 3\,\text{m/s}, 6\,\text{m/s}\}$ and SNR $\in \{0\,\text{dB}, 5\,\text{dB}, 10\,\text{dB}\}$ are depicted in Fig. 14, and 15. The results validate the previous observation.

In the case of STO (c. f. Fig. 14), a smaller spreading factor was more resilient against Doppler shifts. For SF = 6 and *dechirping* (algorithm from Section IV-B), the STO error for 95 % of the estimations (CDF = 95 %) was below 6.7 µs for all velocities and SNRs. Opposed to that, SF = 10 and *dechirping* had a STO error for 95 % of the estimations below 2.1 µs for 0 m/s, 4.2 µs for 1.5 m/s, and 9.8 µs for 3 m/s,whereas 38 % of the estimations yield an STO error below 25 µs at 6 m/s. Surprisingly, the CDF for lower SNR was slightly higher. Presumably, this was to the fact that

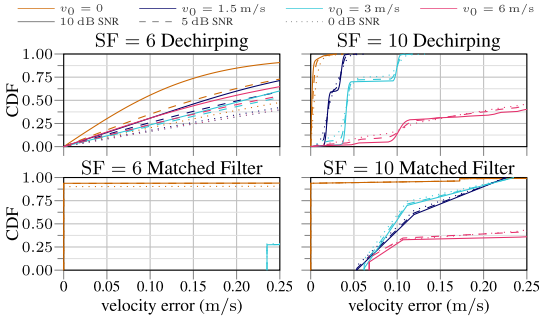

FIGURE 15. CDF of the velocity error. *Dechirping* correspond to the algorithm in Section IV-B, *matched filter* to Section IV-C.

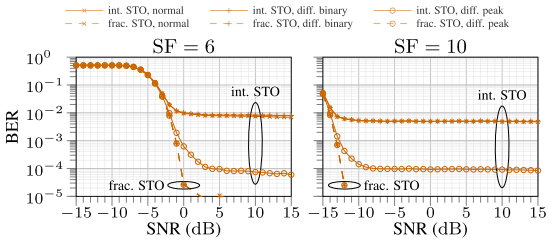

FIGURE 16. Comparison between *integer* (int.) and *integer and fractional* (frac.) STO removal for different symbol codings *normal*, *differential binary* and *differential peak* (c. f. Section IV-E) without Doppler shifts.

middle of the peak is getting lower that the edges. Figure 8b illustrates that for a velocity of 6 m/s. The middle of the peak was at frequency bin 15, but the edges at 13 and 17 were higher. A lower SNR enhanced the probability that bin 15 (or 14 respectively 16) was detected and therefore the estimate had a smaller STO error. For both spreading factors, the *dechirping* had a lower STO error compared to *matched filter* (algorithm from Section IV-C). The stairs in the CDF corresponded to the behavior, that *matched filter* had a resolution of a sample for each SFD symbol. Opposed to that, *dechirping* increased the resolution with a fractional frequency estimator (c. f. Eq. (41)). It is important to note, that an STO error of 25 µs is 0.5 BB sample. In this case, the symbol false detection probability is 50 %, because the energy is equally distributed over two bins (c. f. Fig. 7). A shorter STO than 25 µs increases the probability of a correct symbol detection.

For velocity detection (c. f. Fig. 15), a higher spreading was required. For SF = 10 and *dechirping*, 95 % of the estimations had an velocity error below 15×10^{-3} m/s for 0 m/s, 43×10^{-3} m/s for 1.5 m/s, 106×10^{-3} m/s for 3 m/s and for 6 m/s 40 % of the velocity error was below 250×10^{-3} m/s. A proper velocity detection with SF = 6 and *dechirping* was not possible. Similar to the STO results, *dechirping* was better than *matched filter*.

C. EFFECTS ON THE BER

Finally, the BER was analyzed in different setups:

1) Without Doppler shift to compare fractional and integer-only STO compensation (Fig. 16).

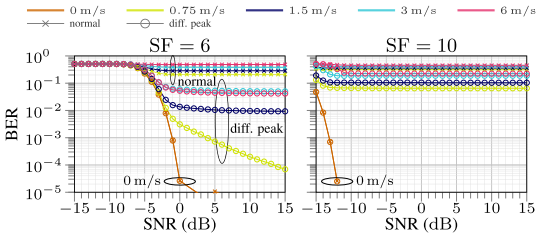

FIGURE 17. Effect of Doppler shifts in the case of STO removal only for different symbol codings *normal* and *differential peak*.

2) With Doppler shift but without Doppler shift compensation (Fig. 17).
3) With Doppler shift and Doppler shift estimation and compensation (Fig. 18).
4) Different differential symbol coding (Fig. 19).
5) Different resampling techniques (Fig. 20).
6) With multiple packet lengths (Fig. 21).
7) Different spreading factors for synchronization (preamble and SFD) and data (Fig. 22).

Unless stated otherwise, each packet carried 64 B randomly generated payload. In our previous paper [20] we observed a saturation of the BER around 10^{-2}. In [20], we compensated integer STO in the BB only. A comparison of different STO compensation methods is given in Fig. 16. After reception of the SFD, the STO was removed (c. f. Section IV-D). First, the integer STO (resulting in a shift of an integer number of BB samples) was considered and afterwards integer and fractional STO (resulting in an interpolation between BB samples). Furthermore, the evaluation considered normal (similar to the LoRa standard, c. f. Section III-B) and differential symbol coding (c. f. Section IV-E). Based on the results in Fig. 16, the BER went into saturation around circa 10^{-2} for normal and differential binary symbol coding. A differential symbol estimation with Eq. 52 improved the BER to 10^{-4}. For all symbol codings, the BER was less than 10^{-5} at 1 dB (SF = 6) respectively −11 dB (SF = 10) SNR. Hence, a fractional and integer STO removal decreased the BER. In the following evaluations, fractional and integer STO was removed.

An integer and fractional STO removal was evaluated in Fig. 17 for different velocities, but without Doppler shift removal to motivate the need of a Doppler shift removal. As derived in Section III-G, a smaller spreading factor is more stable against Doppler shifts. This is proved by the simulation results in Fig. 17. For spreading factor of SF = 6, a differential symbol coding showed some improvements for lower velocities.

The last evaluation showed the requirement of a Doppler shift compensation. The simulation results of our receiving algorithm (c. f. Section IV) with STO and Doppler shift removal is shown in Fig. 18. The Doppler shift and STO were removed in the PB with linear interpolation. In comparison to the results without Doppler shift removal (c. f. Fig. 17), our algorithm showed a strong improvement in the case of

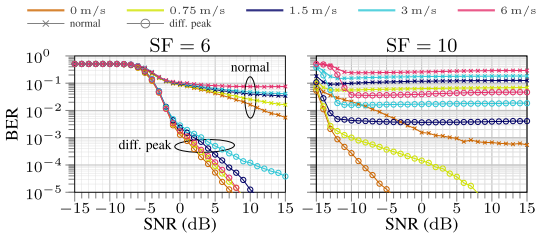

FIGURE 18. Effect of Doppler shifts in the case of STO and Doppler shift removal (interpolation of the PB samples) for different symbol decodings *normal* and *differential peak*.

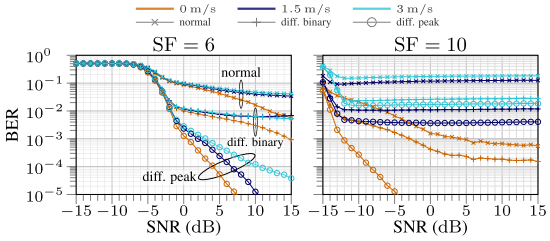

FIGURE 19. Comparison of different symbol decodings *normal*, *differential binary* and *differential peak* (c. f. Section IV-E).

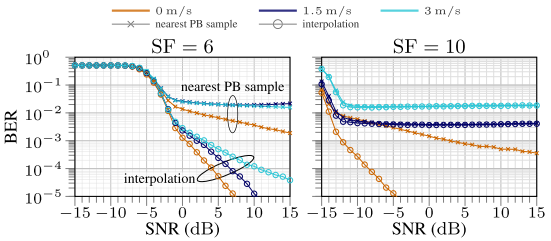

FIGURE 20. Comparison of different STO and Doppler shift removal implementations with *linear interpolation between PB samples* and *the use of the nearest PB sample* (see Section IV-D).

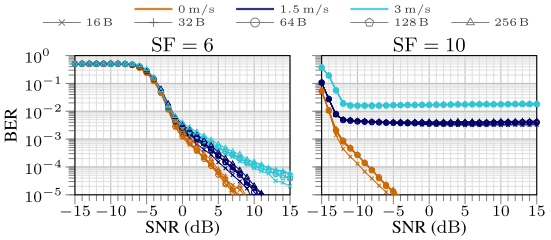

FIGURE 21. Comparision of different payload lengths (16 B, 32 B, 64 B, 128 B, and 256 B) with linear interpolation to remove Doppler shifts and STO and differential peak decoding.

Doppler shifts ($v_0 = \{0.75\,\text{m/s}, 1.5\,\text{m/s}, 3.0\,\text{m/s}, 6.0\,\text{m/s}\}$) for SF $=$ 6 and differential symbol coding. In the case of SF $=$ 10 the Doppler compensation had minor improvements for lower velocities, e. g., $v_0 = 0.75\,\text{m/s}$. On the other hand, the algorithm enhanced the BER in a scenario without Doppler shifts ($v_0 = 0\,\text{m/s}$) compared to the previous evaluation (c. f. Fig. 17). For example, a BER of less than 10^{-5} required a SNR of 1 dB (SF $=$ 6) respectively -11 dB (SF $=$ 10) without Doppler compensation algorithm and 9 dB respectively -4 dB with Doppler compensation in scenarios without Doppler shifts. The difference was a result of estimation errors of the Doppler shift (c. f. Fig. 15).

Section IV-E described different symbol coding implementations, which were compared with simulations. The results shows Fig. 19 for different spreading, SNR and Doppler shifts. In all cases, the differential peak decoding (implementation of Eq. 52) had the lowest BER.

Interpolation required computational resources. Section (IV-D) described methods to remove Doppler shifts and STO. Linear interpolation of the PB samples and the use of the nearest PB sample were compared in Fig. 20. In all cases, linear interpolation had a lower BER.

The effect of Doppler shifts to a packet described Section III-H. During the payload demodulation Doppler shifts produced an increasing or decreasing STO over the time. Therefore, with increasing payload the absolute STO increased. Figure 21 depicts the BER for different payload lengths (16 B, 32 B, 64 B, 128 B, and 256 B). The packet durations were 103 ms, 170 ms, 308 ms, 580 ms, and 1127 ms for SF $=$ 6 and 1190 ms, 1856 ms, 3187 ms, 5798 ms, and 11 020 ms for SF $=$ 10. The differential peak decoding was used and the BER shows minor differences for different payload lengths.

The derivation in Section III-G and the evaluation pointed out that smaller spreading factors were more resilient against Doppler shifts. In general, a high resilience of the modulated data was desirable. On the other hand, for a proper Doppler shift estimation larger spreading factors performed better, because the signals were more effected by Doppler shifts. To fullfil both requirements different spreading factors for preamble and SFD (SF_{sync}) and data transmission (SF_{data}) were implemented. The simulation output shows Fig. 22. In all cases, the data transmission used $\text{SF}_{\text{data}} = 6$. Preamble and SFD were tested with $\text{SF}_{\text{sync}} \in \{7, 8, 9, 10\}$. The gray area in the background of Fig. 22 indicates the BER for $\text{SF}_{\text{sync}} = 6$, $\text{SF}_{\text{data}} = 6$ (c. f. Fig. 18). The usage of a higher spreading for the synchronization resulted in a lower BER. In the best case ($\text{SF}_{\text{sync}} = 10$), a BER below 10^{-5} was reached for 0 m/s and 0.75 m/s at a SNR of -3 dB respectively -2 dB. To archive a similar BER for $\text{SF}_{\text{sync}} = 6$ SNRs of 7 dB respectively 8 dB were required (c. f. Fig. 18). On the other hand, a spreading factor of $\text{SF}_{\text{sync}} = 10$ increased the BER for the highest velocity of 6 m/s due to the inaccurate STO and Doppler shift estimation for large velocities (c. f. Section V-B).

The evaluations pointed out that the presented Doppler shift estimation and compensation algorithm decreased the BER in scenarios with Doppler shifts. Furthermore, differential symbol coding was more resilient against Doppler shifts and STO compared to normal symbol coding. The best performance, w. r. t. the BER, showed a configuration with different spreading factors for synchronization (preamble and SFD) and data transmission. However, there exist a velocity limit for each configuration. The spreading factors

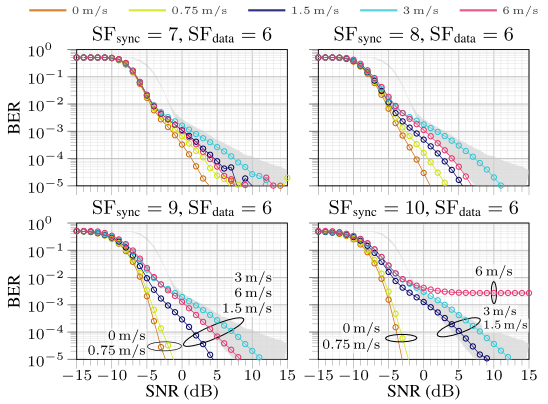

FIGURE 22. Effect of different spreading factors for preamble and STO (SF_{sync}) and data transmission (SF_{data}) with linear interpolation to remove Doppler shifts and STO and differential peak decoding. The gray area in the background indicates the BER for $SF_{sync} = 6$, $SF_{data} = 6$.

must be selected based on the properties of the acoustic communication channel.

VI. CONCLUSION

In this paper, we discussed the effect of Doppler shifts, SFO and STO to FSCM-based low-power acoustic underwater communication. First, we reviewed state-of-art FSCM receiver implementations for RF applications and FSCM and CSS acoustic underwater communication. Due to the low propagation speed of the acoustic wave in the water, Doppler shifts have a strong effect on acoustic underwater communication. We pointed out, that this is the first paper which studies the effect of Doppler shifts in FSCM-based acoustic communication. Furthermore, we derived equations to describe the effect of Doppler shifts to the dechirped FSCM signal. Our findings showed, that smaller spreading factors were more resilient against Doppler shifts. Based on our studies we developed a light-weight synchronization for a joint estimation of Doppler shifts and STO. Moreover, our work contributes to robust transmission schemes such as differential symbol differential symbol coding and different spreading factors for synchronization and data transmission. Finally, we evaluated our algorithm and compared it to a reference algorithm for Doppler tracking. Our algorithm reduced the BER by a factor of more than 10^4 in some cases. For example, we showed that our algorithm improved the BER for a spreading factor of SF = 6 for data transmission at 5 dB SNR and a relative velocity of 0.75 m/s from 2×10^{-1} ($SF_{sync} = SF_{data} = 6$) without Doppler shift compensation to less than 10^{-5} ($SF_{sync} = 10$, $SF_{data} = 6$), respectively from 3×10^{-1} ($SF_{sync} = SF_{data} = 6$) to 10^{-4} ($SF_{sync} = 10$, $SF_{data} = 6$) at 1.5 m/s. It is important to note, that these Doppler shifts were similar to a relative velocity of 1.5×10^5 m/s respectively 3×10^5 m/s in RF communication.

In future work, we plan to evaluate our algorithm in different real-world scenarios with multipath propagation and channel variations. Furthermore, an implementation for the *ahoi* modem is planned to offer the usage of FSCM in μAUVs and UWSNs to advance the research on the IoUT.

APPENDIX A
DERIVATION OF THE EQ. FOR THE UP-DOWN METHOD

A MF or cross-correlation measures the similarity of two signals over the displacement (lag) between each other. In communication systems, MFs measure the similarity between the received signal and a reference signal. The maximum of the MF is the displacement with the highest similarity between received and reference signal.

After the reception of the SFD (two up-chirps and two down-chirps), the four MF peaks $\tau_{p,\nearrow,0}$, $\tau_{p,\nearrow,1}$, $\tau_{p,\searrow,0}$, and $\tau_{p,\searrow,1}$ determine the lag with the highest similarity. The lags are defined w. r. t. the expected lag without STO and Doppler shift. Time shift due to Doppler are defined w. r. t. the begin of the first up-chirp of the SFD.

Based on [44], a Doppler shift produces additional lags for up and down-chirps

$$\tau_{\Delta,\nearrow} = -\tau_{\Delta,\searrow} = -\frac{f_c \Delta T_{sym}}{BW\left(1 + \Delta + \frac{\Delta^2}{2}\right)}. \tag{54}$$

Furthermore, a STO τ shifts the lag $\tau_{\tau,\nearrow} = \tau_{\tau,\searrow} = \tau$.

The four MF peaks can be described with τ_Δ, τ_τ and the time shift per symbol $\tau_{\Delta,T_{sym}} = -T_{sym} \cdot \Delta$.

$$\tau_{p,\nearrow,0} = \tau_{\tau,\nearrow} + \tau_{\Delta,\nearrow} = \tau - \frac{f_c \Delta T_{sym}}{BW\left(1 + \Delta + \frac{\Delta^2}{2}\right)} \tag{55}$$

$$\begin{aligned}\tau_{p,\nearrow,1} &= \tau_{\tau,\nearrow} + \tau_{\Delta,\nearrow} + \tau_{\Delta,T_{sym}} \\ &= \tau - \frac{f_c \Delta T_{sym}}{BW\left(1 + \Delta + \frac{\Delta^2}{2}\right)} - T_{sym} \cdot \Delta\end{aligned} \tag{56}$$

$$\begin{aligned}\tau_{p,\searrow,0} &= \tau_{\tau,\searrow} + \tau_{\Delta,\searrow} + 2 \cdot \tau_{\Delta,T_{sym}} \\ &= \tau + \frac{f_c \Delta T_{sym}}{BW\left(1 + \Delta + \frac{\Delta^2}{2}\right)} - 2T_{sym} \cdot \Delta\end{aligned} \tag{57}$$

$$\begin{aligned}\tau_{p,\searrow,1} &= \tau_{\tau,\searrow} + \tau_{\Delta,\searrow} + 3 \cdot \tau_{\Delta,T_{sym}} \\ &= \tau + \frac{f_c \Delta T_{sym}}{BW\left(1 + \Delta + \frac{\Delta^2}{2}\right)} - 3T_{sym} \cdot \Delta\end{aligned} \tag{58}$$

The equations are rewritten to

$$\begin{aligned}\delta &= \frac{\tau_{p,\nearrow,0} + \tau_{p,\nearrow,1} - \tau_{p,\searrow,0} - \tau_{p,\searrow,1}}{2} \\ &= -\frac{2 f_c \Delta T_{sym}}{BW\left(1 + \Delta + \frac{\Delta^2}{2}\right)} + 2T_{sym} \cdot \Delta \\ &\approx -\frac{2 f_c \Delta T_{sym}}{BW\,(1 + \Delta)} + 2T_{sym} \cdot \Delta\end{aligned} \tag{59}$$

Finally, the Doppler shift is

$$\begin{aligned}\Delta = &-\frac{1}{2}\left(\frac{-f_c}{BW} + 1 - \frac{\delta}{2T_{sym}}\right) \\ &\pm \sqrt{\frac{\left(\frac{-f_c}{BW} + 1 - \frac{\delta}{2T_{sym}}\right)^2}{4} + \frac{\delta}{2T_{sym}}}\end{aligned} \tag{60}$$

To calculate the STO, the Doppler shifts are removed

$$\hat{\tau}_{\mathrm{p},\nearrow,0} = \tau_{\mathrm{p},\nearrow,0} + \frac{f_c \Delta T_{\mathrm{sym}}}{\mathrm{BW}\left(1+\Delta+\frac{\Delta^2}{2}\right)} \tag{61}$$

$$\hat{\tau}_{\mathrm{p},\nearrow,1} = \tau_{\mathrm{p},\nearrow,1} + \frac{f_c \Delta T_{\mathrm{sym}}}{\mathrm{BW}\left(1+\Delta+\frac{\Delta^2}{2}\right)} + T_{\mathrm{sym}} \cdot \Delta \tag{62}$$

$$\hat{\tau}_{\mathrm{p},\searrow,0} = \tau_{\mathrm{p},\searrow,0} - \frac{f_c \Delta T_{\mathrm{sym}}}{\mathrm{BW}\left(1+\Delta+\frac{\Delta^2}{2}\right)} + 2T_{\mathrm{sym}} \cdot \Delta \tag{63}$$

$$\hat{\tau}_{\mathrm{p},\searrow,1} = \tau_{\mathrm{p},\searrow,1} - \frac{f_c \Delta T_{\mathrm{sym}}}{\mathrm{BW}\left(1+\Delta+\frac{\Delta^2}{2}\right)} + 3T_{\mathrm{sym}} \cdot \Delta \tag{64}$$

and averaged

$$\tau = \frac{\hat{\tau}_{\mathrm{p},\nearrow,0} + \hat{\tau}_{\mathrm{p},\nearrow,1} + \hat{\tau}_{\mathrm{p},\searrow,0} + \hat{\tau}_{\mathrm{p},\searrow,1}}{4}. \tag{65}$$

APPENDIX B
LIST OF ACRONYMS

μAUV	Micro autonomous underwater vehicle.
ADC	Analog-to-digital converter.
ADR	Adaptive data rate.
AUV	Autonomous underwater vehicle.
AWGN	Additive white Gaussian noise.
BB	Base band.
BB-SFO	Baseband sampling frequency offset.
BER	Bit error rate.
BFSK	Binary frequency shift keying.
BPF	Band-pass filter.
CDF	Cumulative distribution function.
CFO	Carrier frequency offset.
CSS	Chirp spread spectrum.
DC	Constant component.
DFT	Discrete Fourier transform.
FFT	Fast Fourier transform.
FSCM	Frequency shift chirp modulation.
HFM	Hyperbolic frequency modulation.
IIR	Infinite impulse response.
IoT	Internet of Things.
IoUT	Internet of Underwater Things.
ISI	Inter-symbol interference.
LFM	Iinear frequency modulation.
LLS	Iinear least squares.
LNA	Low-noise amplifier.
LPF	Low-pass filter.
LPWAN	Low-power wide area network.
MAC	Medium access control.
MF	Matched filter.
NLOS	Non-line-of-sight.
PB	Pass band.
PB-SFO	Passband sampling frequency offset.
PHY	Physical.
PLL	Phase-locked loop.
PRR	Packet reception rate.
PSD	Power spectral density.
RF	Radio frequency.
SDR	Software defined radio.
SFD	Starting frame delimiter.
SFO	Sampling frequency offset.
SNR	Signal-to-noise ratio.
STO	Symbol timing offset.
USV	Unmanned surface vehicle.
UWSN	Underwater wireless sensor network.

ACKNOWLEDGMENT

The authors would like to thank Christian Busse for his help to prepare the final version of this article.

REFERENCES

[1] M. Knight and B. Seeber, "Decoding LoRa: Realizing a modern LPWAN with SDR," in *Proc. 6th GNU Radio Conf.*, 2016, pp. 1–5, [Online]. Available: https://pubs.gnuradio.org/index.php/grcon/issue/view/1

[2] R. Ghanaatian, O. Afisiadis, M. Cotting, and A. Burg, "LoRa digital receiver analysis and implementation," in *Proc. IEEE Int. Conf. Acoust., Speech Signal Process. (ICASSP)*, Brighton, U.K., May 2019, pp. 1498–1502, doi: 10.1109/ICASSP.2019.8683504.

[3] J. C. Liando, A. Gamage, A. W. Tengourtius, and M. Li, "Known and unknown facts of LoRa: Experiences from a large-scale measurement study," *ACM Trans. Sensor Netw.*, vol. 15, no. 2, pp. 1–35, May 2019, doi: 10.1145/3293534.

[4] L. Vangelista, "Frequency shift chirp modulation: The LoRa modulation," *IEEE Signal Process. Lett.*, vol. 24, no. 12, pp. 1818–1821, Dec. 2017, doi: 10.1109/LSP.2017.2762960.

[5] C. Bernier, F. Dehmas, and N. Deparis, "Low complexity LoRa frame synchronization for ultra-low power software-defined radios," *IEEE Trans. Commun.*, vol. 68, no. 5, pp. 3140–3152, May 2020, doi: 10.1109/TCOMM.2020.2974464.

[6] T. Ameloot, H. Rogier, M. Moeneclaey, and P. Van Torre, "LoRa signal synchronization and detection at extremely low signal-to-noise ratios," *IEEE Internet Things J.*, vol. 9, no. 11, pp. 8869–8882, Jun. 2022, doi: 10.1109/JIOT.2021.3117039.

[7] M. Xhonneux, O. Afisiadis, D. Bol, and J. Louveaux, "A low-complexity LoRa synchronization algorithm robust to sampling time offsets," *IEEE Internet Things J.*, vol. 9, no. 5, pp. 3756–3769, Mar. 2022, doi: 10.1109/JIOT.2021.3101002.

[8] X. Chen, E. Venosa, and F. Harris, "Synchronization steps for low complexity chirp spread spectrum (CSS) receivers," in *Proc. IEEE Mil. Commun. Conf. (MILCOM)*, San Diego, CA, USA, Nov. 2021, pp. 127–132, doi: 10.1109/MILCOM52596.2021.9652971.

[9] F. Campagnaro, F. Steinmetz, and B.-C. Renner, "Survey on low-cost underwater sensor networks: From niche applications to everyday use," *J. Mar. Sci. Eng.*, vol. 11, no. 1, p. 125, Jan. 2023, doi: 10.3390/jmse11010125.

[10] S. A. H. Mohsan, A. Mazinani, N. Q. H. Othman, and H. Amjad, "Towards the Internet of Underwater Things: A comprehensive survey," *Earth Sci. Informat.*, vol. 15, no. 2, pp. 735–764, Jun. 2022, doi: 10.1007/s12145-021-00762-8.

[11] C. Osterloh, T. Pionteck, and E. Maehle, "MONSUN II: A small and inexpensive AUV for underwater swarms," in *Proc. 7th German Conf. Robot.*, Munich, Germany, May 2012, pp. 1–6.

[12] D. A. Duecker, N. Bauschmann, T. Hansen, E. Kreuzer, and R. Seifried, "HippoCampusX—A hydrobatic open-source micro AUV for confined environments," in *Proc. IEEE/OES Auto. Underwater Vehicles Symp. (AUV)*, St. Johns, NL, Canada, Sep. 2020, pp. 1–6, doi: 10.1109/AUV50043.2020.9267949.

[13] S. Iacoponi, G. J. Van Vuuren, G. Santaera, N. Mankovskii, I. Zhilin, F. Renda, C. Stefanini, and G. D. Masi, "H-SURF: Heterogeneous swarm of underwater robotic fish," in *Proc. Oceans*, Hampton Roads, VA, USA, Oct. 2022, pp. 1–5, doi: 10.1109/OCEANS47191.2022.9977253.

[14] N. Morozs, P. D. Mitchell, Y. Zakharov, R. Mourya, Y. R. Petillot, T. Gibney, M. Dragone, B. Sherlock, J. A. Neasham, C. C. Tsimenidis, M. E. Sayed, A. C. McConnell, S. Aracri, and A. A. Stokes, "Robust TDA-MAC for practical underwater sensor network deployment: Lessons from USMART sea trials," in *Proc. 13th ACM Int. Conf. Underwater Netw. Syst.*, Shenzhen, China, Dec. 2018, pp. 1–8, doi: 10.1145/3291940.3291970.

[15] T. Zainab, J. Karstens, and O. Landsiedel, "Cross-domain fusion in smart seafloor sensor networks," *Informatik Spektrum*, vol. 45, no. 5, pp. 290–294, Oct. 2022, doi: 10.1007/s00287-022-01486-9.
[16] Y. Yang, R. Elsinghorst, J. J. Martinez, H. Hou, J. Lu, and Z. D. Deng, "A real-time underwater acoustic telemetry receiver with edge computing for studying fish behavior and environmental sensing," *IEEE Internet Things J.*, vol. 9, no. 18, pp. 17821–17831, Sep. 2022, doi: 10.1109/JIOT.2022.3164092.
[17] E. Coccolo, C. Delea, F. Steinmetz, R. Francescon, A. Signori, C. N. Au, F. Campagnaro, V. Schneider, F. Favaro, J. Oeffner, B.-C. Renner, and M. Zorzi, "System architecture and communication infrastructure for the RoboVaaS project," *IEEE J. Ocean. Eng.*, vol. 48, no. 3, pp. 716–739, Jul. 2023, doi: 10.1109/JOE.2023.3234710.
[18] Z. Zhang, Y. Xiao, Z. Ma, M. Xiao, Z. Ding, X. Lei, G. K. Karagiannidis, and P. Fan, "6G wireless networks: Vision, requirements, architecture, and key technologies," *IEEE Veh. Technol. Mag.*, vol. 14, no. 3, pp. 28–41, Sep. 2019, doi: 10.1109/MVT.2019.2921208.
[19] C.-X. Wang, J. Huang, H. Wang, X. Gao, X. You, and Y. Hao, "6G wireless channel measurements and models: Trends and challenges," *IEEE Veh. Technol. Mag.*, vol. 15, no. 4, pp. 22–32, Dec. 2020, doi: 10.1109/MVT.2020.3018436.
[20] F. Steinmetz and B.-C. Renner, "Taking LoRa for a dive: CSS for low-power acoustic underwater communication," in *Proc. 6th Underwater Commun. Netw. Conf. (UComms)*, Lerici, Italy, Aug. 2022, pp. 1–5, doi: 10.1109/UComms56954.2022.9905674.
[21] B.-C. Renner, J. Heitmann, and F. Steinmetz, "AHOI: Inexpensive, low-power communication and localization for underwater sensor networks and μAUVs," *ACM Trans. Sensor Netw.*, vol. 16, no. 2, pp. 1–46, May 2020, doi: 10.1145/3376921.
[22] J. Hermans, G. Sklivanitis, and D. A. Pados, "A first-of-its-kind low size, weight and power run-time reconfigurable underwater modem," in *Proc. 6th Underwater Commun. Netw. Conf. (UComms)*, Lerici, Italy, Aug. 2022, pp. 1–5, doi: 10.1109/UComms56954.2022.9905700.
[23] J. Potter, J. Alves, D. Green, G. Zappa, I. Nissen, and K. McCoy, "The Janus underwater communications standard," in *Proc. Underwater Commun. Netw. (UComms)*, Sestri Levante, Italy, Sep. 2014, pp. 1–4, doi: 10.1109/UComms.2014.7017134.
[24] M. Centenaro, L. Vangelista, A. Zanella, and M. Zorzi, "Long-range communications in unlicensed bands: The rising stars in the IoT and smart city scenarios," *IEEE Wireless Commun.*, vol. 23, no. 5, pp. 60–67, Oct. 2016, doi: 10.1109/MWC.2016.7721743.
[25] Blue Robotics Inc. (Nov. 16, 2023). *BlueROV2*. [Online]. Available: https://bluerobotics.com/store/rov/bluerov2/
[26] A. A. Doroshkin, A. M. Zadorozhny, O. N. Kus, V. Y. Prokopyev, and Y. M. Prokopyev, "Experimental study of LoRa modulation immunity to Doppler effect in CubeSat radio communications," *IEEE Access*, vol. 7, pp. 75721–75731, 2019, doi: 10.1109/ACCESS.2019.2919274.
[27] J. Petäjäjärvi, K. Mikhaylov, M. Pettissalo, J. Janhunen, and J. Iinatti, "Performance of a low-power wide-area network based on LoRa technology: Doppler robustness, scalability, and coverage," *Int. J. Distrib. Sensor Netw.*, vol. 13, no. 3, Mar. 2017, Art. no. 155014771769941, doi: 10.1177/1550147717699412.
[28] D. Patel and M. Won, "Experimental study on low power wide area networks (LPWAN) for mobile Internet of Things," in *Proc. IEEE 85th Veh. Technol. Conf. (VTC Spring)*, Sydney, NSW, Australia, Jun. 2017, pp. 1–5, doi: 10.1109/VTCSpring.2017.8108501.
[29] T. Ameloot, M. Moeneclaey, P. Van Torre, and H. Rogier, "Characterizing the impact of Doppler effects on body-centric LoRa links with SDR," *Sensors*, vol. 21, no. 12, p. 4049, Jun. 2021, doi: 10.3390/s21124049.
[30] P. Robyns, P. Quax, W. Lamotte, and W. Thenaers, "A multi-channel software decoder for the LoRa modulation scheme," in *Proc. 3rd Int. Conf. Internet Things, Big Data Secur.*, Madeira, Portugal, 2018, pp. 1–11, doi: 10.5220/0006668400410051.
[31] M. A. Ben Temim, G. Ferré, and R. Tajan, "A novel approach to enhance the robustness of LoRa-like PHY layer to synchronization errors," in *Proc. IEEE Global Commun. Conf.*, Taipei, Taiwan, Dec. 2020, pp. 1–6, doi: 10.1109/GLOBECOM42002.2020.9322210.
[32] J. Tapparel, O. Afisiadis, P. Mayoraz, A. Balatsoukas-Stimming, and A. Burg, "An open-source LoRa physical layer prototype on GNU radio," in *Proc. IEEE 21st Int. Workshop Signal Process. Adv. Wireless Commun. (SPAWC)*, Atlanta, GA, USA, May 2020, pp. 1–5, doi: 10.1109/SPAWC48557.2020.9154273.
[33] M. Rezzouki, M. A. B. Temim, and G. Ferré, "Differential chirp spread spectrum to perform acoustic long range underwater localization and communication," in *Proc. Oceans*, San Diego, CA, USA, Sep. 2021, pp. 1–9, doi: 10.23919/OCEANS44145.2021.9706010.
[34] M. Rezzouki and G. Ferré, "Design and implementation of differential chirp spread spectrum system for underwater acoustic communication," in *Proc. Oceans*, Hampton Roads, VA, USA, Oct. 2022, pp. 1–7, doi: 10.1109/OCEANS47191.2022.9977293.
[35] Z. Jia, W. Zheng, and F. Yuan, "A two-dimensional chirp-MFCSK modulation method for underwater LoRa system," *IEEE Internet Things J.*, vol. 9, no. 23, pp. 24388–24397, Dec. 2022, doi: 10.1109/JIOT.2022.3188755.
[36] Elektor International Media B.V. (Dec. 2013). *Smart Meter Transceiver IC Has Range of 15 km*. [Online]. Available: https://www.elektormagazine.com/news/smart-meter-transceiver-ic-has-range-of-15-km
[37] L. Slats, Semtech Corporation. (Jan. 2020). *A Brief History of LoRa: Three Inventors Share Their Personal Story at The Things Conference*. [Online]. Available: https://blog.semtech.com/a-brief-history-of-lora-three-inventors-share-their-personal-story-at-the-things-conference
[38] LoRa Developer Portal, Semtech Corporation. (Nov. 16, 2023). *Implementing Adaptive Data Rate (ADR)*. [Online]. Available: https://lora-developers.semtech.com/documentation/tech-papers-and-guides/implementing-adaptive-data-rate-adr/implementing-adaptive-data-rate/
[39] C. Yang and G. Wei, "A noniterative frequency estimator with rational combination of three spectrum lines," *IEEE Trans. Signal Process.*, vol. 59, no. 10, pp. 5065–5070, Oct. 2011, doi: 10.1109/TSP.2011.2160257.
[40] E. Jacobsen and P. Kootsookos, "Fast, accurate frequency estimators [DSP tips & tricks]," *IEEE Signal Process. Mag.*, vol. 24, no. 3, pp. 123–125, May 2007, doi: 10.1109/msp.2007.361611.
[41] M. Johnson, L. Freitag, and M. Stojanovic, "Improved Doppler tracking and correction for underwater acoustic communications," in *Proc. IEEE Int. Conf. Acoust., Speech, Signal Process.*, Munich, Germany, Apr. 1997, pp. 575–578, doi: 10.1109/icassp.1997.599703.
[42] B. S. Sharif, J. Neasham, O. R. Hinton, and A. E. Adams, "A computationally efficient Doppler compensation system for underwater acoustic communications," *IEEE J. Ocean. Eng.*, vol. 25, no. 1, pp. 52–61, Jan. 2000, doi: 10.1109/48.820736.
[43] G. Zappa, I. Nissen, and J. Potter, "Doppler compensation for JANUS applied to data collected in the Baltic Sea," in *Proc. 4th UAM Conf.*, Kos island, Greece, 2011, pp. 1–8.
[44] R. Diamant, A. Feuer, and L. Lampe, "Choosing the right signal: Doppler shift estimation for underwater acoustic signals," in *Proc. 7th ACM Int. Conf. Underwater Netw. Syst.*, Los Angeles, CA, USA, Nov. 2012, pp. 1–8, doi: 10.1145/2398936.2398971.
[45] C. Baldone, G. E. Galioto, D. Croce, I. Tinnirello, and C. Petrioli, "Doppler estimation and correction for Janus underwater communications," in *Proc. IEEE Global Commun. Conf.*, Taipei, Taiwan, Dec. 2020, pp. 1–6, doi: 10.1109/GLOBECOM42002.2020.9348220.
[46] M. Stojanovic and J. Preisig, "Underwater acoustic communication channels: Propagation models and statistical characterization," *IEEE Commun. Mag.*, vol. 47, no. 1, pp. 84–89, Jan. 2009, doi: 10.1109/mcom.2009.4752682.
[47] P. A. van Walree, "Propagation and scattering effects in underwater acoustic communication channels," *IEEE J. Ocean. Eng.*, vol. 38, no. 4, pp. 614–631, Oct. 2013, doi: 10.1109/JOE.2013.2278913.
[48] F. Steinmetz, J. Heitmann, and C. Renner, "A practical guide to chirp spread spectrum for acoustic underwater communication in shallow waters," in *Proc. 13th ACM Int. Conf. Underwater Netw. Syst.*, Shenzhen, China, Dec. 2018, doi: 10.1145/3291940.3291964.
[49] Y. Su, L. Dong, Z. Zhou, X. Liu, and X. Wei, "A general embedded underwater acoustic communication system based on advance STM32," *IEEE Embedded Syst. Lett.*, vol. 13, no. 3, pp. 90–93, Sep. 2021, doi: 10.1109/LES.2020.3006838.
[50] E. Coccolo, F. Campagnaro, D. Tronchin, A. Montanari, R. Francescon, L. Vangelista, and M. Zorzi, "Underwater acoustic modem for a Morphing distributed autonomous underwater vehicle (MODA)," in *Proc. Oceans*, Chennai, India, Feb. 2022, pp. 1–8, doi: 10.1109/oceanschennai45887.2022.9775308.
[51] J. A. Neasham, G. Goodfellow, and R. Sharphouse, "Development of the 'Seatrac' miniature acoustic modem and USBL positioning units for subsea robotics and diver applications," in *Proc. Oceans*, Genova, Italy, May 2015, pp. 1–8, doi: 10.1109/oceans-genova.2015.7271578.
[52] D. J. Schott, A. Gabbrielli, W. Xiong, G. Fischer, F. Höflinger, J. Wendeberg, C. Schindelhauer, and S. J. Rupitsch, "Asynchronous chirp slope keying for underwater acoustic communication," *Sensors*, vol. 21, no. 9, p. 3282, May 2021, doi: 10.3390/s21093282.

[53] K. G. Kebkal and R. Bannasch, "Sweep-spread carrier for underwater communication over acoustic channels with strong multipath propagation," *J. Acoust. Soc. Amer.*, vol. 112, no. 5, pp. 2043–2052, Nov. 2002, doi: 10.1121/1.1504855.

[54] L. Marchetti and R. Reggiannini, "An efficient receiver structure for sweep-spread-carrier underwater acoustic links," *IEEE J. Ocean. Eng.*, vol. 41, no. 2, pp. 440–449, Apr. 2016, doi: 10.1109/JOE.2015.2445251.

[55] P. A. van Walree, F.-X. Socheleau, R. Otnes, and T. Jenserud, "The watermark benchmark for underwater acoustic modulation schemes," *IEEE J. Ocean. Eng.*, vol. 42, no. 4, pp. 1007–1018, Oct. 2017, doi: 10.1109/JOE.2017.2699078.

[56] F. Steinmetz and B.-C. Renner, "From the long-range channel in the ocean to the short-range and very shallow-water acoustic channel in ports and harbors," in *Proc. 5th Underwater Commun. Netw. Conf. (UComms)*, Lerici, Italy, Aug. 2021, pp. 1–5, doi: 10.1109/UComms50339.2021.9598094.

[57] A. Pozzebon, I. Cappelli, F. Campagnaro, R. Francescon, and M. Zorzi, "LoRaWAN transmissions in salt water for superficial marine sensor networking: Laboratory and field tests," *Sensors*, vol. 23, no. 10, p. 4726, May 2023, doi: 10.3390/s23104726.

[58] C.-T. Chen and F. J. Millero, "Speed of sound in seawater at high pressures," *J. Acoust. Soc. Amer.*, vol. 62, no. 5, pp. 1129–1135, Nov. 1977, doi: 10.1121/1.381646.

[59] I. F. Akyildiz, D. Pompili, and T. Melodia, "Underwater acoustic sensor networks: Research challenges," *Ad Hoc Netw.*, vol. 3, no. 3, pp. 257–279, May 2005, doi: 10.1016/j.adhoc.2005.01.004.

[60] J. Heidemann, W. Ye, J. Wills, A. Syed, and Y. Li, "Research challenges and applications for underwater sensor networking," in *Proc. IEEE Wireless Commun. Netw. Conf., WCNC.*, Las Vegas, NV, USA, Apr. 2006, pp. 228–235, doi: 10.1109/wcnc.2006.1683469.

[61] M. Stojanovic, "On the relationship between capacity and distance in an underwater acoustic communication channel," in *Proc. 1st ACM Int. Workshop Underwater Netw.*, Los Angeles, CA, USA, 2006, pp. 34–43, doi: 10.1145/1161039.1161049.

[62] R. J. Urick, *Principles of Underwater Sound*. Los Altos, CA, USA: Peninsula, 1996.

[63] R. P. Hodges, *Underwater Acoustics: Analysis, Design and Performance of Sonar*. Hoboken, NJ, USA: Wiley, 2010.

[64] F. Steinmetz and C. Renner, "Resilience against shipping noise and interference in low-power acoustic underwater communication," in *Proc. Oceans*, Seattle, WA, USA, Oct. 2019, pp. 1–10, doi: 10.23919/OCEANS40490.2019.8962790.

[65] E. Coccolo, F. Campagnaro, A. Signori, F. Favaro, and M. Zorzi, "Implementation of AUV and ship noise for link quality evaluation in the DESERT underwater framework," in *Proc. 13th ACM Int. Conf. Underwater Netw. Syst.*, Shenzhen, China, Dec. 2018, pp. 1–8, doi: 10.1145/3291940.3291966.

[66] P. A. van Walree and R. Otnes, "Ultrawideband underwater acoustic communication channels," *IEEE J. Ocean. Eng.*, vol. 38, no. 4, pp. 678–688, Oct. 2013, doi: 10.1109/JOE.2013.2253391.

[67] B. Binnerts, K. Blom, and S. Giodini, "Analysis of underwater acoustic propagation in a harbour environment and its effect on communication," in *Proc. Oceans*, Jun. 2017, pp. 1–6, doi: 10.1109/OCEANSE.2017.8084628.

[68] M. Chitre, T.-B. Koay, G. Deane, and G. Chua, "Variability in shallow water communication performance near a busy shipping lane," in *Proc. 5th Underwater Commun. Netw. Conf. (UComms)*, Lerici, Italy, Aug. 2021, pp. 1–5, doi: 10.1109/UComms50339.2021.9598017.

[69] W. H. Press, S. A. Teukolsky, W. T. Vetterling, and B. P. Flannery, *Numerical Recipes in C: The Art of Scientific Computing*, 2nd ed. Cambridge, U.K.: Cambridge Univ. Press, 2002.

FABIAN STEINMETZ (Graduate Student Member, IEEE) received the B.Sc. and M.Sc. degrees in electrical engineering from the Hamburg University of Technology (TUHH), in 2015 and 2018, respectively, where he is currently pursuing the Ph.D. degree. Afterward, he joined the Research Group smartPORT, TUHH. From 2021 to 2022, he was with the Institute of Computer Science, University of Koblenz–Landau. In 2022, he returned to TUHH and started with the Institute for Autonomous Cyber-Physical Systems. He is a Research Assistant with TUHH. His current work involves acoustic underwater communication and localization for low-power applications, for example underwater wireless sensor networks or micro autonomous underwater vehicles. Furthermore, he was involved in the MarTERA RoboVaaS Project. In 2018, he received the Best Paper Award from the International Conference on Underwater Networks and Systems (WUWNet).

BERND-CHRISTIAN RENNER received the Diploma and Ph.D. degrees from the Hamburg University of Technology (TUHH), in 2008 and 2013, respectively. From 2012 to 2016, he was a Postdoctoral Researcher with the University of Lübeck. From 2016 to 2020, he was an Assistant Professor with TUHH. From 2020 to 2022, he was an Associate Professor with the University of Koblenz–Landau. He is currently a Full Professor and the Head of the Institute for Autonomous Cyber-Physical Systems (ACPS), TUHH. He has published papers in several international journals and conferences. His research interests include applications of networked low-power sensing and cyber-physical systems running on energy harvested from the environment, networking protocols for networks of embedded sensors, and active and passive backscatter acoustic communication, localization, and navigation in mobile, low-power underwater networks. He reviewed for and served on several TPCs. He has been serving the ENSsys Workshop at ACM SenSys in several roles, since 2014, and is a member of its steering committee.